

# Three-body boundary-corrected continuum-intermediate-state method for single charge exchange with the general transition amplitude ( $1s \rightarrow nlm$ ) applied to the $p$ -H( $1s$ ), $\alpha$ -H( $1s$ ), and $p$ -He( $1s^2$ ) collisions with $n \leq 4$

Nenad Milojević<sup>1</sup>, Ivan Mančev<sup>1</sup>, Danilo Delibašić<sup>1</sup>, and Dževad Belkić<sup>2,3</sup>

<sup>1</sup>*Department of Physics, Faculty of Sciences and Mathematics, University of Niš, P.O. Box 224, 18000 Niš, Serbia*

<sup>2</sup>*Department of Oncology-Pathology, Karolinska Institute, P.O. Box 260, SE-171 76 Stockholm, Sweden*

<sup>3</sup>*Radiation Physics and Nuclear Medicine, Karolinska University Hospital, SE-171 76 Stockholm, Sweden*



(Received 19 February 2020; accepted 6 July 2020; published 27 July 2020)

We derive a general quantum-mechanical transition amplitude in the prior version of the three-body boundary-corrected continuum-intermediate-state (BCIS-3B) method for single charge exchange in collisions of heavy nuclei with atomic hydrogenlike targets. The obtained expression is valid for all the transitions from the initial ground to any final hydrogenlike bound states ( $1s \rightarrow nlm$ ), where  $\{n, l, m\}$  is the usual triple of the quantum numbers (principal, angular, magnetic). The outcome is semianalytical: a judicious combination of an analytical calculation (as far as feasible) and the subsequent numerical computations (quadrature for integrals that could not be reduced to closed formulas). The final results for the  $T$ -matrix elements are a compact double integration computed by numerical quadratures over real variables in finite intervals. The ensuing total cross section is a single numerical quadrature of the squared absolute value of this transition amplitude integrated over the magnitude of the transverse momentum transfer vector. This can provide detailed information on the cross sections for each individual subshell  $\{n, l, m\}$  of the newly formed hydrogenlike atom or ion comprised of a projectile nucleus and the captured electron. Using these general expressions, we computed a large number of state-selective and state-summed cross sections (both differential and total) for electron capture in the  $p$ -H,  $\alpha$ -H, and  $p$ -He collisions at intermediate and high impact energies. The energy dependence of the cross sections for the individual shells and their subshells with the fixed quantum numbers  $n$ ,  $\{n, l\}$ , and  $\{n, l, m\}$  are reported via detailed tables and figures. Also, differential cross sections (state selective and summed) are computed for the  $p$ -H collisions at 60, 125, and 5000 keV. All the present results from the BCIS-3B method are found to be in very good agreement with the existing experimental data on differential and total cross sections, both state selective (whenever available) and state summed. The provided cross-section database can find important applications in several investigative fields ranging from plasma physics, astrophysics, and heavy-ion transport physics through fusion research and technology to hadron therapy.

DOI: [10.1103/PhysRevA.102.012816](https://doi.org/10.1103/PhysRevA.102.012816)

## I. INTRODUCTION

Abundant applications of different perturbative [1–6] and nonperturbative [7–14] methods for studying the problem of charge exchange in ion-atom collisions at intermediate and high impact energies have a long history, dating back to the pioneering work of Oppenheimer [15] as well as Brinkman and Kramers [16]. The most significant developments with a lasting effect to the current times have been carried out with the methods fulfilling the correct boundary conditions in both scattering channels. In a review paper [1], a long-standing issue was resolved concerning the often misunderstood role of the internuclear Coulomb interaction potential. This was made possible by understanding and appreciating the importance of the correct Coulomb boundary conditions as the working solution of the well-known asymptotic convergence problem [1,17,18].

Such conditions consist of a simultaneous requirement for the correct asymptotic behaviors of the scattering wave functions in the entrance as well as exit channels and the proper introduction of the corresponding perturbation interactions

that produce the transitions from the initial to the final states of the system. In other words, it is not permitted to choose a total scattering wave function by ignoring its relationship with the corresponding perturbation potential in the given transition amplitude. Overlooking this provision resulted in many misleading publications in the past, as reviewed in Refs. [1–5]. In particular, Ref. [1] is known for several very important results. Among these is the general proof that the internuclear Coulomb potential does not contribute to the exact eikonal total cross sections. Moreover, a notable byproduct contained in the exact eikonal transition amplitude is the three-body boundary-corrected first Born (CB1-3B) method. The introduction of this proper first-order perturbation theory from Ref. [1] conclusively resolved the well-known and long-standing controversy about the Oppenheimer-Brinkman-Kramers (OBK) versus Jackson-Schiff-Bates-Dalgarno (JSBD) first-order perturbative approximations for charge exchange. The former approximation has then been discarded as being never adequate, whereas the latter one was finally understood to be fortuitously correct only for a single case of electron capture from atomic hydrogen by protons. Hereafter,

the clause “eikonal” implies a dominant contribution from forward-scattered heavy projectiles due to negligible electron-nuclei mass ratios,  $\sim 10^{-4}$  or smaller.

In the CB1-3B method, the boundary-correct scattering state vectors  $\Phi_{i,f}^{\pm}$  are given by the product of the unperturbed channel states  $\Phi_{i,f}$  and the logarithmic distortion phases  $\mathcal{L}_{i,f}^{\pm}$  due to the Coulomb long-range remainders  $V_{i,f}^{\infty}$  of the perturbation potentials  $V_{i,f}$ . These Coulomb phases  $\mathcal{L}_{i,f}^{\pm}$  for the relative motions of heavy nuclei are consistent with the short-range distorting potentials  $V_{i,f}^{(\text{CB1-3B})} = V_{i,f} - V_{i,f}^{\infty}$ . Here,  $V_{i,f}^{\infty}$  are the asymptotic expressions of the channel perturbations  $V_{i,f}$  when the scattering particles are located at infinite separations  $R$  from each other. Thus, in the convenient notation of Ref. [5], the prior and post transition amplitudes in the CB1-3B method are given by the  $T$ -matrix elements:

$$\text{Prior : } T_{if}^{(\text{CB1-3B})-} = \langle \Phi_f^- | \xi_i^{(\text{CB1-3B})+} \rangle, \quad \xi_i^{(\text{CB1-3B})+} = V_i^{(\text{CB1-3B})} \Phi_i^+, \quad (1)$$

$$\text{Post : } T_{if}^{(\text{CB1-3B})+} = \langle \xi_f^{(\text{CB1-3B})-} | \Phi_i^+ \rangle, \quad \xi_f^{(\text{CB1-3B})-} = V_f^{(\text{CB1-3B})} \Phi_f^-, \quad (2)$$

respectively. The CB1-3B method was successfully applied to many single-capture collisions [19–39]. This method has generally been found to be in very good agreement with the existing experimental data at intermediate and high impact energies, below the region where the classical Thomas double scattering becomes important. Double scattering of the electron with the two nuclei is not included in the CB1-3B method, where capture is mediated by a single collisional mechanism via direct encounters of the electron with the projectile nucleus.

Among the second-order formalisms, the two-center three-body continuum-distorted-wave (CDW-3B) method [18] is very frequently employed. This is a high-energy, symmetric, boundary-correct approximation. The CDW-3B method shows a consistent success in a large number of tests against measured total cross sections. Here, the unperturbed channel states  $\Phi_{i,f}$  are distorted by the full continuum waves associated with the interactions of the electron with the projectile and target nuclei in the entrance and exit channels, respectively. The prior and post transition amplitudes in this method are defined as  $T_{if}^{(\text{CDW-3B})-} = \langle \chi_f^{(\text{CDW-3B})-} | \{V_i - V_i^{(\text{CDW-3B})}\} \chi_i^{(\text{CDW-3B})+} \rangle$  and  $T_{if}^{(\text{CDW-3B})+} = \langle \chi_f^{(\text{CDW-3B})-} | \{V_f - V_f^{(\text{CDW-3B})}\} \chi_i^{(\text{CDW-3B})+} \rangle$ , respectively. The distorting potentials  $V_{i,f}^{(\text{CDW-3B})}$  are expressed as the difference between the channel perturbations  $V_{i,f}$  and the nonlocal potential operators  $U_{i,f}^{(\text{CDW-3B})} = \vec{\nabla}_{x,s} \ln \varphi_{i,f} \cdot \vec{\nabla}_{s,x}$ , so that

$$\text{Prior : } T_{if}^{(\text{CDW-3B})-} = \langle \chi_f^{(\text{CDW-3B})-} | \xi_i^{(\text{CDW-3B})+} \rangle, \quad (3)$$

$$\xi_i^{(\text{CDW-3B})+} = U_i^{(\text{CDW-3B})} \chi_i^{(\text{CDW-3B})+},$$

$$\text{Post : } T_{if}^{(\text{CDW-3B})+} = \langle \xi_f^{(\text{CDW-3B})-} | \chi_i^{(\text{CDW-3B})+} \rangle,$$

$$\xi_f^{(\text{CDW-3B})-} = U_f^{(\text{CDW-3B})} \chi_f^{(\text{CDW-3B})-}. \quad (4)$$

The associated distorted waves  $\chi_{i,f}^{(\text{CDW-3B})\pm}$  are the products of bound states  $\varphi_{i,f}$  and the two full Coulomb waves (one for the electronic and the other for the nuclear motions). In the

eikonal mass limit for the relative motions of heavy nuclei, the initial and final Coulomb waves due to the electrostatic internuclear potential reduce to their asymptotic phases that disappear from the total cross sections [1]. We see here that a consistent application of the eikonal hypothesis has practical advantages. One of them is that the full Coulomb waves for the relative motion of heavy nuclei can safely be replaced by their eikonal logarithmic phase factors, as also done in the CB1-3B method as well as in other first- and second-order theories.

The three-body boundary-corrected continuum-intermediate-state (BCIS-3B) method is another second-order theory which has recently been employed in Ref. [40] for one-electron capture from the  $K$  shell of multielectron atomic targets (carbon, nitrogen, oxygen, neon, and argon) by bare projectiles (the nuclei of H, He, and Li) at intermediate and high impact energies. In the transition amplitude of the prior BCIS-3B method, the perturbation potential and the distorted wave in the entrance channel are the same as in the CB1-3B method, whereas the distorted wave in the exit channel coincides with that of the CDW-3B method. On the other hand, in the transition amplitude of the post BCIS-3B method, the perturbation potential and the distorted wave in the exit channel are the same as in the CB1-3B method, whereas the distorted wave in the entrance channel is identical to that of the CDW-3B method. As such, the prior and post transition amplitudes in the BCIS-3B method are defined as  $T_{if}^{(\text{BCIS-3B})-} = \langle \chi_f^{(\text{CDW-3B})-} | V_f^{(\text{BCIS-3B})} | \Phi_i^+ \rangle$  and  $T_{if}^{(\text{BCIS-3B})+} = \langle \Phi_f^- | V_f^{(\text{BCIS-3B})} | \chi_i^{(\text{CDW-3B})+} \rangle$ , where  $V_{i,f}^{(\text{BCIS-3B})} = V_{i,f}^{(\text{CB1-3B})}$ , respectively. Thus,

$$\text{Prior : } T_{if}^{(\text{BCIS-3B})-} = \langle \chi_f^{(\text{CDW-3B})-} | \xi_i^{(\text{CB1-3B})+} \rangle, \quad (5)$$

$$\text{Post : } T_{if}^{(\text{BCIS-3B})+} = \langle \xi_f^{(\text{CB1-3B})-} | \chi_i^{(\text{CDW-3B})+} \rangle. \quad (6)$$

This writing, following Ref. [5], transparently shows that the BCIS-3B method is a hybridization of the CDW-3B and CB1-3B methods in either the prior or post transition amplitudes.

The forerunner of this formalism is the three-body continuum-intermediate-state (CIS-3B) method for charge exchange between bare nuclei and hydrogenlike atomic systems [41]. The CIS-3B method satisfies the correct boundary conditions in one channel (entrance or exit, depending on whether the post or the prior form of the transition amplitude is used). In the complementary channel (say, entrance, for the prior form) with no electronic distortion, the CIS-3B method replaces the boundary-correct distortion  $\mathcal{L}_i^+$  in  $\Phi_i^+$  by the boundary-incorrect Coulomb logarithmic phase due to the internuclear potential alone  $V_{P,T}$ . As a consequence, the initial perturbation  $V_i$  becomes a physically unjustifiable long-range potential (the Coulomb electrostatic interaction between the target electron and the projectile nucleus). The CIS-3B method has been used in various applications [42–45], to cite only a few. It has subsequently been renamed to the three-body target-continuum-distorted-wave (TCDW-3B) method [46–49]. A variant of the CIS-3B or, equivalently, TCDW-3B method from Refs. [42–49] has recently been extended to four-body systems and applied to various charge-exchange collisions [50–52].

In fact, it was first within four-body problems that the one-center boundary-correct hybrid methods with continuum intermediate states have been introduced. This was the four-body boundary-corrected continuum-intermediate-state (BCIS-4B) method for double-electron capture in collisions of fast heavy nuclei with heliumlike atomic systems [53]. Afterward, the BCIS-4B method has been adapted and successfully applied to single-electron capture from heliumlike atomic systems by bare projectiles [54]. Thus far, both the BCIS-3B [40] and BCIS-4B [53,54] methods have been employed only in conjunction with the ground-to-ground state capture. A large number of theoretical studies have been performed using different four-body methods for various one- and two-electron transitions in collisions of completely stripped projectiles and heliumlike atomic systems or in collisions between two hydrogenlike atoms or ions [3–5,55].

The main goal of this work is to generalize the BCIS-3B method to single-electron capture by a bare projectile from a ground-state hydrogenlike atomic system into the final arbitrary hydrogenlike shells and subshells  $\{n, l, m\}$  of the transferred electron. Another goal is to critically assess the validity and utility of the BCIS-3B method by comparing the obtained results with the available measurements, for state-selective and total cross sections as well as for differential cross sections at intermediate and high impact energies. We also compare some of our differential and total cross sections with the corresponding results from the recent close-coupling-type computations [9–11].

Especially at sufficiently high impact energies, classical double Thomas scattering yields significant contributions and it is, therefore, important to evaluate the pertinent predictions by the BCIS-3B method. This is motivated by the fact that this approximation contains a quantum-mechanical counterpart of the Thomas classical billiard-type double scattering. An important mechanism for a rearrangement collision is the classical Thomas double scattering through two successive elastic encounters of the electron on the two nuclei (both through  $60^\circ$ ). A quantum-mechanical double scattering described in the BCIS-3B method proceeds first by ionizing the target electron and then capturing it from an on-shell continuum state. The signature of double scattering, within an angular distribution, is the second-order peak (the Thomas peak) which at sufficiently high impact energies dominates over the first-order, forward peak.

The outcomes of the present computations are from the realm of a charge-changing cross-section database which is of a notable practical interest not only to atomic collision physics, but also to plasma physics, astrophysics, and heavy-ion transport physics. Moreover, such databases can find useful applications in other interdisciplinary areas, ranging from fusion energy research [56–59] to medical physics (cancer therapy by high-energy heavy ions) [60–68]. In all these fields, charge-changing cross sections play an important role in estimations of energy losses of ions during their passage through matter of varying kind, including tissue of patients during radiotherapy treatments.

Atomic units will be used throughout unless otherwise stated.

## II. THEORY

### A. Purely three-body charge-exchange problems

We examine single-electron capture in collisions of a nucleus P of mass  $M_P$  and charge  $Z_P$  (projectile) with hydrogenlike atomic systems (target) consisting of an electron  $e$  bound to the nucleus T of mass  $M_T$  and charge  $Z_T$  :

$$Z_P + (Z_T, e)_i \longrightarrow (Z_P, e)_f + Z_T, \quad (7)$$

where the parentheses symbolize the bound states that are presently taken as  $i = 1s$  (ground) and  $f = \{n, l, m\}$  (ground, excited). The set  $\{n, l, m\}$  represents the usual triple of the hydrogenlike quantum numbers (principal, angular, magnetic). Let  $\vec{s}$  and  $\vec{x}$  be the position vectors of the electron relative to the nuclei P and T, respectively. Further, let  $\vec{R} = \vec{x} - \vec{s}$  be the position vector of P with respect to T. Moreover, by  $\vec{r}_i$  and  $\vec{r}_f$  we shall denote the position vectors of P and T with respect to the center of mass of the systems  $(Z_T, e)_i$  and  $(Z_P, e)_f$ , respectively.

According to (5), the prior form of the transition amplitude for (7) in the BCIS-3B method reads as

$$T_{if}^{(\text{BCIS-3B})-} \equiv T_{if}^{(\text{BCIS-3B})} = \langle \chi_f^- | V_i - V_i^\infty | \Phi_i^+ \rangle. \quad (8)$$

Since the post form will not be used, the minus superscript will hereafter be dropped from the transition amplitude and cross sections, where  $V_i - V_i^\infty$  is the distorting potential in the entrance channel. This interaction has two long-range components  $V_i = Z_P Z_T / R - Z_P / s$  and  $V_i^\infty = Z_P (Z_T - 1) / R$  where the latter is the asymptote (at  $R \rightarrow \infty$ ) of the former. The  $e$ -P distance  $s$  reduces to the P-T distance  $R$  at infinitely large values of  $R$ , so that

$$V_i - V_i^\infty = \frac{Z_P Z_T}{R} - \frac{Z_P}{s} - \frac{Z_P (Z_T - 1)}{R} = \frac{Z_P}{R} - \frac{Z_P}{s}. \quad (9)$$

The Coulomb-distorted initial and final scattering wave functions in the entrance and exit channels are

$$\Phi_i^+ = \varphi_i(\vec{x}) e^{i\vec{k}_i \cdot \vec{r}_i + i\nu_i \ln(vR - \vec{v} \cdot \vec{R})}, \quad (10)$$

$$\begin{aligned} \chi_f^- = & \varphi_{nlm}(\vec{s}) e^{-i\vec{k}_f \cdot \vec{r}_f - i\nu_{PT} \ln(vR + \vec{v} \cdot \vec{R})} N^-(\nu_\tau) \\ & \times {}_1F_1(-i\nu_\tau, 1, -i\nu x - i\vec{v} \cdot \vec{x}), \end{aligned} \quad (11)$$

where  $\nu_i = Z_P(Z_T - 1)/v$ ,  $N^-(\nu_\tau) = \Gamma(1 + i\nu_\tau) e^{\pi\nu_\tau/2}$ ,  $\nu_\tau = Z_T/v$ , and  $\nu_{PT} = Z_P Z_T / v$ . Vector  $\vec{v}$  (directed along the  $Z$  axis in a fixed XOYZ system,  $\hat{v} = \hat{Z}$ ) is the velocity vector of the projectile in the laboratory frame of reference. Symbols  $\Gamma$  and  ${}_1F_1(a, b, z)$  denote the gamma and the confluent hypergeometric function [69,70]. Functions  $\varphi_i(\vec{x})$  and  $\varphi_{nlm}(\vec{s})$  represent the bound-state wave functions of the one-electron atomic systems  $(Z_T, e)_i$  and  $(Z_P, e)_f$  with binding energies  $E_i = -Z_T^2/2$  and  $E_f = -Z_P^2/(2n^2)$ , where  $i = 1s$ , as stated. Quantities  $\vec{k}_i$  and  $\vec{k}_f$  are the initial and final wave vectors. By definition,  $\vec{k}_i$  is the momentum of P with respect to  $(Z_T, e)_i$ , whereas  $\vec{k}_f$  is the momentum of  $(Z_P, e)_f$  relative to T. This convention yields the initial and final plane waves  $e^{i\vec{k}_i \cdot \vec{r}_i}$  and  $e^{-i\vec{k}_f \cdot \vec{r}_f}$ , respectively. The function  $\varphi_{\vec{v}}^-(\vec{x}) = N^-(\nu_\tau) e^{-i\vec{v} \cdot \vec{x}} {}_1F_1(-i\nu_\tau, 1, -i\nu x - i\vec{v} \cdot \vec{x})$  from (11) is the electronic continuum Coulomb wave function due to the attractive electrostatic field  $V_\tau = -Z_T/x$ .

It describes intermediate ionization of the electron  $e$  by the impact of  $P$  onto the target. The plane wave  $e^{-i\vec{v}\cdot\vec{x}}$  from  $\varphi_{\vec{v}}^{-}(\vec{x})$  does not explicitly appear in (11) because it is immersed into the final plane wave  $e^{-i\vec{k}_f\cdot\vec{r}_f}$  of the exit-channel unperturbed state  $\Phi_f = \varphi_{nlm}(\vec{s}) e^{-i\vec{k}_f\cdot\vec{r}_f}$ . Using the eikonal hypothesis, the product of the logarithmic Coulomb phases from the functions  $\Phi_i^+$  and  $\chi_f^-$  can be reduced to a single  $\vec{R}$ -dependent phase factor

$$\begin{aligned} & e^{i\nu_i \ln(\nu R - \vec{v}\cdot\vec{R})} \{ e^{-i\nu_{PT} \ln(\nu R + \vec{v}\cdot\vec{R})} \}^* \\ & = (\rho\nu)^{2iZ_p(Z_T-1)/\nu} (\nu R + \vec{v}\cdot\vec{R})^{i\xi}. \end{aligned} \quad (12)$$

Here,  $\xi = Z_p/\nu$  and  $\vec{\rho}$  is the vectorial component of the vector  $\vec{R}$  in the XOY plane ( $\vec{\rho} = \vec{R} - \vec{Z}$ ,  $\vec{\rho}\cdot\vec{Z} = 0$ ). The multiplying term  $(\rho\nu)^{2iZ_p(Z_T-1)/\nu}$  comes from the Coulomb repulsion between  $Z_p$  and  $Z_T - 1$  that is  $V_i^\infty = Z_p(Z_T - 1)/R$ . This  $\rho$ -dependent phase does not contribute to the total cross sections for any values  $Z_p$  and  $Z_T$  [68]. For a hydrogen atom as a target ( $Z_T = 1$ ), the term  $(\rho\nu)^{2iZ_p(Z_T-1)/\nu}$  is equal to unity. In such a case, differential cross sections in the BCIS-3B method become directly proportional the square of the absolute value of the transition amplitudes. This obviates the need for the numerically difficult Fourier-Bessel highly oscillatory integral (over  $\rho \in [0, \infty]$ ) in differential cross sections from the BCIS-3B method. These obstacles are caused by the Bessel functions arising from integration over the azimuthal angles of the  $\vec{\rho}$ -dependent transition amplitude which itself is the Fourier transform of the corresponding  $\vec{\eta}$ -dependent  $T$ -matrix element [68]. By contrast, the Fourier-Bessel integration must be performed numerically in the differential cross sections

from, e.g., the CDW-3B method for any value of the nuclear charges, including  $Z_p = 1$  and/or  $Z_T = 1$  [1].

With the outlined setting, the prior form of the transition amplitude (8) can be rewritten as

$$\begin{aligned} T_{if}^{(\text{BCIS-3B})-} & \equiv T_{if}(\vec{\eta}) \\ & = N^{-*}(\nu_T) \iint d\vec{s} d\vec{R} \varphi_{nlm}^*(\vec{s}) \left( \frac{Z_p}{R} - \frac{Z_p}{s} \right) \varphi_i(\vec{x}) \\ & \quad \times e^{i\vec{\beta}\cdot\vec{R} - i\vec{v}\cdot\vec{s}} {}_1F_1(i\nu_T, 1, i\nu x + i\vec{v}\cdot\vec{x}) (\nu R + \vec{v}\cdot\vec{R})^{i\xi}. \end{aligned} \quad (13)$$

In the eikonal formalism for heavy-particle collisions, the argument  $\vec{k}_i\cdot\vec{r}_i + \vec{k}_f\cdot\vec{r}_f$  in the plane-wave product  $e^{i\vec{k}_i\cdot\vec{r}_i} (e^{-i\vec{k}_f\cdot\vec{r}_f})^*$  takes the following standard form which with the full account of the electron translation factor

$$\vec{k}_i\cdot\vec{r}_i + \vec{k}_f\cdot\vec{r}_f = \vec{\beta}\cdot\vec{R} - \vec{v}\cdot\vec{s} = -\vec{\alpha}\cdot\vec{R} - \vec{v}\cdot\vec{x}, \quad (14)$$

$$\vec{\alpha} = \vec{\eta} - \left( \frac{v}{2} - \frac{\Delta E}{v} \right) \hat{v}, \quad \vec{\beta} = -\vec{\eta} - \left( \frac{v}{2} + \frac{\Delta E}{v} \right) \hat{v},$$

$$\vec{\alpha} + \vec{\beta} = -\vec{v}, \quad \Delta E = E_i - E_f. \quad (15)$$

Here,  $\vec{\eta} = (\eta \cos \phi_\eta, \eta \sin \phi_\eta, 0)$  is the transverse momentum transfer vector ( $\vec{\eta}\cdot\vec{v} = 0$ ).

### B. Analytical calculations of a part of the three-body transition amplitude

For the confluent hypergeometric function  ${}_1F_1(a, c, z)$ , we use its customary integral representation with the real variable  $t$  [71]

$${}_1F_1(a, c, z) = \frac{\Gamma(c)}{\Gamma(a)\Gamma(c-a)} \int_0^1 dt t^{a-1} (1-t)^{c-a-1} e^{zt}, \quad \text{Re}(c) > \text{Re}(a) > 0. \quad (16)$$

The convergence condition  $\text{Re}(c) > \text{Re}(a) > 0$  of this integral for the present case  ${}_1F_1(i\nu_T, 1, i\nu x + i\vec{v}\cdot\vec{x})$  is secured by redefining the Sommerfeld parameter  $\nu_T$  as  $\nu_T - i\epsilon$ . Here,  $\epsilon > 0$  is an infinitesimally small positive number, which is set to zero once the calculation has been completed. Then, the transition amplitude (13) is calculated as

$$T_{if}(\vec{\eta}) = \mathcal{M} \int_0^1 d\tau f(\tau) \mathcal{K}_{if}(\tau), \quad (17)$$

$$f(\tau) = \tau^{i\nu_T-1} (1-\tau)^{-i\nu_T}, \quad \mathcal{M} = \frac{N^{-*}(\nu_T)}{\Gamma(i\nu_T)\Gamma(1-i\nu_T)} = \frac{e^{\pi\nu_T/2}}{\Gamma(i\nu_T)}, \quad (18)$$

$$\mathcal{K}_{if}(\tau) = \int d\vec{R} e^{i\vec{\beta}\cdot\vec{R}} (\nu R + \vec{v}\cdot\vec{R})^{i\xi} \mathcal{P}(\vec{R}), \quad (19)$$

$$\mathcal{P}(\vec{R}) = \frac{Z_p(Z_T)^{3/2}}{\sqrt{\pi}} \int d\vec{s} \varphi_{nlm}^*(\vec{s}) e^{-i\vec{v}\cdot\vec{s}} \left( \frac{1}{R} - \frac{1}{s} \right) e^{-Z_T x + i(\nu x + \vec{v}\cdot\vec{x})\tau}. \quad (20)$$

From here on, Ref. [28] will be closely followed. In Ref. [28], using the CB1-3B approximation for process (7), with any initial  $i = \{n^i, l^i, m^i\}$  and final  $f = \{n^f, l^f, m^f\}$  hydrogenic quantum numbers, a general semianalytical method has been developed to calculate the post and prior transition amplitudes  $T_{if}^{(\text{CB1})\pm}$ . This original method has subsequently been extended to the four-body boundary-corrected first Born (CB1-4B) approximation for one-electron capture by heavy nuclei from heliumlike atomic targets [72].

Thus, with the help of the Fourier transform  $e^{-Z_\tau x + i(vx + \vec{v} \cdot \vec{x})\tau} = \mu_\tau \pi^{-2} \int d\vec{q} e^{-i\vec{q} \cdot \vec{x}} (q_1^2 + \mu_\tau^2)^{-2}$ , where  $\mu_\tau = Z_\tau - i v \tau$  and  $\vec{q}_1 = \vec{q} + \vec{v} \tau$ , we have

$$\mathcal{P}(\vec{R}) = Z_p \left[ \frac{1}{R} W_R(\vec{R}) - W_s(\vec{R}) \right], \tag{21}$$

$$W_R(\vec{R}) = \mu_\tau \sqrt{\frac{Z_\tau^3}{\pi^5}} \int d\vec{q} \frac{e^{-i\vec{q} \cdot \vec{R}}}{(q_1^2 + \mu_\tau^2)^2} \mathcal{B}, \quad W_s(\vec{R}) = \mu_\tau \sqrt{\frac{Z_\tau^3}{\pi^5}} \int d\vec{q} \frac{e^{-i\vec{q} \cdot \vec{R}}}{(q_1^2 + \mu_\tau^2)^2} \mathcal{C}, \tag{22}$$

$$\mathcal{B} = \int d\vec{s} e^{-i(\vec{v} + \vec{q}) \cdot \vec{s}} \varphi_{nlm}^*(\vec{s}) = \int d\vec{s} e^{-i(\vec{v} + \vec{q}) \cdot \vec{s}} \int d\vec{q}_2 e^{i\vec{q}_2 \cdot \vec{s}} \tilde{\varphi}_{nlm}^*(\vec{q}_2), \tag{23}$$

$$\mathcal{C} = \int d\vec{s} e^{-i(\vec{v} + \vec{q}) \cdot \vec{s}} \frac{\varphi_{nlm}^*(\vec{s})}{s} = \int d\vec{s} e^{-i(\vec{v} + \vec{q}) \cdot \vec{s}} \int d\vec{q}_2 e^{i\vec{q}_2 \cdot \vec{s}} \tilde{\chi}_{nlm}^*(\vec{q}_2). \tag{24}$$

The momentum-space wave functions  $\tilde{\varphi}_{nlm}(\vec{q}_2)$  and  $\tilde{\chi}_{nlm}(\vec{q}_2)$  are the Fourier transforms of  $\varphi_{nlm}(\vec{s})$  and  $\chi_{nlm}(\vec{s}) = \varphi_{nlm}(\vec{s})/s$ , i.e.,  $\tilde{\varphi}_{nlm}(\vec{q}_2) = (2\pi)^{-3} \int d\vec{s} e^{i\vec{q}_2 \cdot \vec{s}} \varphi_{nlm}(\vec{s})$  and  $\tilde{\chi}_{nlm}(\vec{q}_2) = (2\pi)^{-3} \int d\vec{s} e^{i\vec{q}_2 \cdot \vec{s}} \chi_{nlm}(\vec{s})$ . For the present calculation, the particularly convenient form of the momentum distribution function  $\tilde{\varphi}_{nlm}(\vec{q}_2)$  is taken from Refs. [28,73] as

$$\tilde{\varphi}_{nlm}(\vec{q}_2) = (2\pi)^{-3} N_f^{Z_p} i^l \sum_{p=0}^{n_r} C_p \frac{\mathcal{Y}_{lm}(\vec{q}_2)}{(q_2^2 + a_f^2)^{p+l+2}}, \tag{25}$$

$$\tilde{\chi}_{nlm}(\vec{q}_2) = (2\pi)^{-3} \frac{N_f^{Z_p}}{2Z_p} i^l \sum_{p=0}^{n_r} C_p \frac{\mathcal{Y}_{lm}(\vec{q}_2)}{(q_2^2 + a_f^2)^{p+l+1}}, \tag{26}$$

$$N_f^{Z_p} = 16\pi Z_p \left[ \frac{a_f^3}{n} \frac{(n+l)!}{n_r!} \right]^{1/2} \frac{l!(4a_f)^l}{(2l+1)!}, \tag{27}$$

$$C_p = \frac{(-n_r)_p (n+l+1)_p}{(l+3/2)_p p!} a_f^{2p}, \quad n_r = n-l-1, \quad a_f = \frac{Z_p}{n}. \tag{28}$$

The regular solid harmonic denoted by  $\mathcal{Y}_{lm}$  is defined by  $\mathcal{Y}_{lm}(\vec{q}_2) = q_2^l Y_{lm}(\hat{q}_2)$ , where  $Y_{lm}(\hat{q}_2)$  is the spherical harmonic, whereas  $(a)_k$  is the Pochhammer symbol  $(a)_k = a(a+1)(a+2) \dots (a+k-1)$  with  $(a)_0 = 1$ . Now, the integrals  $\mathcal{B}$  and  $\mathcal{C}$  acquire the forms

$$\mathcal{B} = (2\pi)^{-3} N_f^{Z_p} (-i)^l \sum_{p=0}^{n_r} C_p \int d\vec{q}_2 \frac{\mathcal{Y}_{lm}^*(\vec{q}_2)}{(q_2^2 + a_f^2)^{p+l+2}} \int d\vec{s} e^{-i(\vec{v} + \vec{q} - \vec{q}_2) \cdot \vec{s}}, \tag{29}$$

$$\mathcal{C} = (2\pi)^{-3} \frac{N_f^{Z_p}}{2Z_p} (-i)^l \sum_{p=0}^{n_r} C_p \int d\vec{q}_2 \frac{\mathcal{Y}_{lm}^*(\vec{q}_2)}{(q_2^2 + a_f^2)^{p+l+1}} \int d\vec{s} e^{-i(\vec{v} + \vec{q} - \vec{q}_2) \cdot \vec{s}}. \tag{30}$$

Using the Dirac delta function and setting  $\vec{q} \rightarrow \vec{q} + \vec{\beta}$ , the integrals  $W_R(\vec{R})$  and  $W_s(\vec{R})$  are reduced to

$$W_R(\vec{R}) = \mu_\tau \sqrt{\frac{Z_\tau^3}{\pi^5}} N_f^{Z_p} (-i)^l \sum_{p=0}^{n_r} C_p \mathcal{G}_p^{(2)}(\vec{R}), \tag{31}$$

$$W_s(\vec{R}) = \mu_\tau \sqrt{\frac{Z_\tau^3}{\pi^5}} \frac{N_f^{Z_p}}{2Z_p} (-i)^l \sum_{p=0}^{n_r} C_p \mathcal{G}_p^{(1)}(\vec{R}), \tag{32}$$

$$\mathcal{G}_p^{(j)}(\vec{R}) = e^{-i\vec{\beta} \cdot \vec{R}} \int d\vec{q} e^{-i\vec{q} \cdot \vec{R}} \frac{\mathcal{Y}_{lm}^*(\vec{q} - \vec{\alpha})}{(|\vec{q} - \vec{\alpha}|^2 + a_f^2)^{p+l+j} (|\vec{q} + \vec{\beta}_1|^2 + \mu_\tau^2)^2} \quad (j = 1, 2), \tag{33}$$

where  $\vec{\beta}_1 = \vec{\beta} + \vec{v} \tau$ ,  $\vec{\alpha} + \vec{\beta}_1 = -\vec{v}_1$ , and  $\vec{v}_1 = \vec{v}(1 - \tau)$ . The two denominators in the integral (33) can be collected into a single denominator by way of the usual Feynman parametrization integral [28]

$$\frac{1}{A^u B^r} = \frac{(u+r-1)!}{(u-1)!(r-1)!} \int_0^1 dt \frac{t^{u-1} (1-t)^{r-1}}{[At + B(1-t)]^{u+r}} \quad (u, r \geq 1), \tag{34}$$

$$\mathcal{G}_p^{(j)}(\vec{R}) = (p+l+j+1)(p+l+j) \int_0^1 dt t^{p+l+j-1} (1-t) \mathcal{U}_p^{(j)}(\vec{R}), \tag{35}$$

$$\begin{aligned} \mathcal{U}_p^{(j)}(\vec{R}) &= e^{-i\vec{\beta} \cdot \vec{R}} \int d\vec{q} e^{-i\vec{q} \cdot \vec{R}} \frac{\mathcal{Y}_{lm}^*(\vec{q} - \vec{\alpha})}{[ (|\vec{q} - \vec{\alpha}|^2 + a_f^2)t + (|\vec{q} + \vec{\beta}_1|^2 + \mu_\tau^2)(1-t) ]^{p+l+j+2}} \\ &= e^{-i\vec{Q}_\beta \cdot \vec{R}} \int d\vec{q} e^{-i\vec{q} \cdot \vec{R}} \frac{\mathcal{Y}_{lm}^*(\vec{q} + \vec{Q}_\alpha)}{(q^2 + \Delta^2)^{p+l+j+2}}. \end{aligned} \tag{36}$$

Here, we redefine  $\vec{q}$  as  $\vec{q} \rightarrow \vec{q} + \vec{Q}$ , so that

$$\vec{Q} = \vec{\alpha}t - \vec{\beta}_1(1-t), \quad \vec{Q}_\alpha = \vec{Q} - \vec{\alpha} = (1-t)\vec{v}_1, \tag{37}$$

$$\vec{Q}_\beta = \vec{Q} + \vec{\beta} = [(\tau-1)t - \tau]\vec{v}, \quad \Delta^2 = v_1^2 t(1-t) + a_f^2 t + \mu_\tau^2(1-t). \tag{38}$$

From the general results of a protracted analytical calculation in Ref. [28], we extract the presently relevant expressions for  $i = \{1, 0, 0\}$  and  $f = \{n, l, m\}$ :

$$\mathcal{U}_p^{(j)}(\vec{R}) = \frac{\pi^{5/2}}{2^{n_j-2} n_j!} e^{-i\vec{Q}_\beta \cdot \vec{R}} \sum_{\lambda_1=|m|}^l (-i)^{\lambda_1} (1-t)^{\lambda_2} \Omega(\lambda_1, v) \frac{B_{\nu_j \lambda_1, -m}^{(\Delta)}(\vec{R})}{\Delta^{2n_j-2\lambda_1-1}}, \tag{39}$$

$$\mathcal{G}_p^{(j)}(\vec{R}) = \frac{\pi^{5/2}}{2^{n_j-2} (n_j-2)!} \sum_{\lambda_1=|m|}^l (-i)^{\lambda_1} \Omega(\lambda_1, v) \int_0^1 dt t^{n_j-2} (1-t)^{\lambda_2+1} e^{-i\vec{Q}_\beta \cdot \vec{R}} \frac{B_{\nu_j \lambda_1, -m}^{(\Delta)}(\vec{R})}{\Delta^{2n_j-2\lambda_1-1}}, \tag{40}$$

$$\lambda_1 + \lambda_2 = l, \quad \nu_j = n_j - \lambda_1, \quad n_j = n + j - 2, \quad n = p + l + 3, \tag{41}$$

$$\Omega(\lambda_1, v) = \frac{(-1)^m}{\sqrt{4\pi}} (\lambda_1 |lm) v^{\lambda_2} (1-\tau)^{\lambda_2}, \tag{42}$$

$$(\lambda_1 |lm) = \left[ \frac{(2l+1)}{(2\lambda_1+1)} \frac{(l+m)!}{(\lambda_1+m)!} \frac{(l-m)!}{(\lambda_1-m)!(\lambda_2!)^2} \right]^{1/2}. \tag{43}$$

Here,  $B_{\nu_j \lambda_1, -m}^{(\Delta)}(\vec{R}) = \hat{k}_{\nu_j-1/2}(R\Delta) \mathcal{Y}_{\lambda_1, -m}(\vec{R})$  is the so-called  $B$  function [74] where  $\hat{k}_{\nu_j-1/2}(R\Delta) = \sqrt{2/\pi} (R\Delta)^{\nu_j-1/2} K_{\nu_j-1/2}(R\Delta)$  is the reduced Bessel function and  $K_{\nu_j-1/2}(R\Delta)$  is the McDonald function [69]. Both  $\hat{k}_{n\pm 1/2}(z)$  and  $K_{n\pm 1/2}(z)$  are polynomials in powers of  $1/z$  ( $n = 0, 1, 2, \dots$ ). The substitution of (40) into Eqs. (31) and (32), followed by the use of (21), maps  $\mathcal{K}_{if}(\tau)$  from Eq. (19) into the expression

$$\mathcal{K}_{if}(\tau) = \mu_\tau Z_p(Z_\tau)^{3/2} (-i)^l N_f^{Z_p} \sum_{p=0}^{n_r} \frac{C_p}{2^{n-2} (n-2)!} \sum_{\lambda_1=|m|}^l (-i)^{\lambda_1} \Omega(\lambda_1, v) \int_0^1 dt \frac{t^{p+l} (1-t)^{\lambda_2+1}}{\Delta^{2n-2\lambda_1-3}} \left[ \frac{t}{\Delta^2} I_0^{(p, \lambda_1)} - \frac{n-2}{Z_p} I_1^{(p, \lambda_1)} \right], \tag{44}$$

$$I_\delta^{(p, \lambda_1)} = \int d\vec{R} (vR + \vec{v} \cdot \vec{R})^{i\xi} e^{-i\vec{Q} \cdot \vec{R}} B_{\nu_{2-\delta} \lambda_1, -m}^{(\Delta)}(\vec{R}) R^{\delta-1}; \quad \delta = 0, 1. \tag{45}$$

At last, a lengthy calculation of the integral  $I_\delta^{(p, \lambda_1)}$  from Ref. [28] gives the final result

$$I_\delta^{(p, \lambda_1)} = 4\pi (-1)^{\lambda_1} (2i)^{\lambda_1} \frac{(2\{n_p - \delta\})!}{(n_p - \delta)!} \sum_{p_r=0}^{n_p-\delta} \frac{(\delta - n_p)_{p_r}}{(2\{\delta - n_p\})_{p_r}} \frac{2^{\delta+p_r-n_p}}{p_r!} \Delta^{p_r} G_{p_r \lambda_1, -m}^{(\delta, \Delta)}(\vec{Q}), \tag{46}$$

$$G_{p_r \lambda_1, -m}^{(\delta, \Delta)}(\vec{Q}) = \sum_{k=0}^{p_\delta} \sum_{l_1=|m|}^{\lambda_1} \Phi_{kl_1}(\delta) \mathcal{D}_{l_1, -m}(\vec{Q} \cdot \vec{v}), \tag{47}$$

$$n_p = n - \lambda_1 - 1, \quad p_\delta = p_r + \delta. \tag{48}$$

The remaining quantities in Eq. (47) are defined by

$$\mathcal{D}_{l_1, -m}(\vec{Q} \cdot \vec{v}) = (l_1 | \lambda_1 m) (-iv)^{l_2} \mathcal{Y}_{l_1, -m}(\vec{Q}), \tag{49}$$

$$(l_1 | \lambda_1 m) = \left[ \frac{(2\lambda_1+1)}{(2l_1+1)} \frac{(\lambda_1+m)!}{(l_1+m)!} \frac{(\lambda_1-m)!}{(l_1-m)!(l_2!)^2} \right]^{1/2}, \tag{50}$$

$$\Phi_{kl_1}(\delta) = (a_\delta b_\delta) {}_3F_2(-k_\delta/2, -k_\delta/2 + 1/2, 1 - i\gamma_1; k + \lambda_1 + 1, -p_\delta - \lambda_1; 1/A), \tag{51}$$

$$a_\delta = \Gamma(1 + i\xi) (\lambda_1 + 1)_{p_\delta} \frac{(2D)^{p_\delta}}{(\Delta^2 + Q^2)^{\lambda_1}} \mathcal{F}, \tag{52}$$

$$b_\delta = \frac{(1 + i\xi)_{l_1} (-i\xi)_{l_2} (-p_\delta)_k (i\gamma_2)_k (-1)^k C^k}{B^{l_2} (\lambda_1 + 1)_k k!}, \tag{53}$$

$${}_3F_2(-k_\delta/2, -k_\delta/2 + 1/2, 1 - i\gamma_1; k + \lambda_1 + 1, -p_\delta - \lambda_1; 1/A) = \sum_{u=0}^{\lfloor k_\delta/2 \rfloor} \frac{(-k_\delta/2)_u (-k_\delta/2 + 1/2)_u (1 - i\gamma_1)_u}{(k + \lambda_1 + 1)_u (-p_\delta - \lambda_1)_u u!} \left(\frac{1}{A}\right)^u, \tag{54}$$

$$A = \frac{\Delta^2}{\Delta^2 + Q^2}, \quad B = \frac{2(v\Delta - i\vec{Q} \cdot \vec{v})}{\Delta^2 + Q^2}, \quad C = \frac{v}{B\Delta} - 1, \tag{55}$$

$$D = \frac{A}{\Delta}, \quad \mathcal{F} = \frac{B^{i\xi}}{\Delta^2 + Q^2}, \tag{56}$$

$$k_\delta = p_\delta - k, \quad l_1 + l_2 = \lambda_1, \quad \gamma_1 = -\xi + il_1, \quad \gamma_2 = -\xi - il_2. \tag{57}$$

Here,  $[k_\delta/2]$  is the largest integer contained in the fraction  $k_\delta/2$ . The symbol  ${}_3F_2$  denotes the Clausen generalized hypergeometric function [75]  ${}_3F_2(a_1, a_2, a_3; b_1, b_2; z) = \sum_{k=0}^\infty \{[(a_1)_k(a_2)_k(a_3)_k]/[(b_1)_k(b_2)_k]\} z^k/k!$  ( $|z| < 1$ ) whose much simpler, polynomial form (54) has been derived in Ref. [28].

With the outlined intermediate expressions, the transition amplitude  $T_{if}$ , as the defining original six-dimensional integral, is transformed into a two-dimensional integral over the real variables  $\tau$  and  $t$

$$T_{if}(\vec{\eta}) = \mathcal{N} \int_0^1 d\tau f(\tau) \mu_\tau \sum_{p=0}^{n_r} \sum_{\lambda_1=|m|}^l (-2)^{\lambda_1} C_p \Omega(\lambda_1, v) [J_0^{(\lambda_1, p_r)} - J_1^{(\lambda_1, p_r)}], \tag{58}$$

$$\mathcal{N} = 16\pi Z_p Z_T^3 (-i)^l \frac{e^{\pi v_\tau/2}}{\Gamma(iv_\tau)}. \tag{59}$$

Here,  $J_\delta^{(\lambda_1, p_r)}$  is a one-dimensional integral over  $t$

$$J_\delta^{(\lambda_1, p_r)} = \frac{(2\{n_p - \delta\})! N_f^{Z_p}}{2^n Z_p^\delta (n - 2 - \delta)! (n_p - \delta)!} \sum_{p_r=0}^{n_p - \delta} \frac{(\delta - n_p)_{p_r}}{(2\{\delta - n_p\})_{p_r}} \frac{2^{p_r + \delta - n_p}}{p_r!} \int_0^1 dt \frac{t^{n - \delta - 2} (1 - t)^{\lambda_2 + 1}}{\Delta^{2n - 2\lambda_1 - p_r - 2\delta - 1}} G_{p_r, \lambda_1, -m}^{(\delta, \Delta)}(\vec{Q}). \tag{60}$$

The differential and total cross sections are defined by

$$\frac{dQ_{if}}{d\Omega} \left( \frac{a_0^2}{\text{sr}} \right) = \frac{\mu^2}{4\pi^2} |T_{if}(\vec{\eta})|^2, \tag{61}$$

$$Q_{if}(\pi a_0^2) = \frac{1}{2\pi^2 v^2} \int_0^\infty d\eta \eta |T_{if}(\vec{\eta})|^2, \tag{62}$$

where  $\mu = M_p M_T / (M_p + M_T)$  is the reduced mass of  $M_p$  and  $M_T$ . In the BCIS-3B method, neither the total nor differential cross section depend on the sign of the magnetic quantum number  $m$ . The two-dimensional Gauss-Legendre quadratures, as two successive one-dimensional Gauss-Legendre quadratures each with the known (tabulated) pivots and weights, are utilized for the numerical integration over  $t$  and  $\tau$ . The Cauchy regularization was applied to the integration over  $\tau$  [53,54] before applying the Gauss-Legendre quadrature. The remaining Gauss-Legendre numerical integration over  $\eta$  is performed using a variable change  $\eta = (1 + x)\sqrt{2/(1 - x^2)}$ , where  $x \in [-1, +1]$ . This change is very important for heavy projectiles since it concentrates the integration points near the forward cone, which gives the dominant contribution to the total cross sections [29].

### C. Effective three-body charge-exchange problems in four-particle collisions

The entire analysis from Secs. II A and II B can only minimally be modified to become directly applicable to single charge exchange in purely four-body problems of the type

$$Z_p + (Z_T; e_1, e_2)_{1s^2} \rightarrow (Z_p, e_1)_{f_1} + (Z_T, e_2)_{f_2}, \tag{63}$$

where  $f_1$  and  $f_2$  are the triples of the usual quantum numbers (principal, angular, magnetic) of the two hydrogenlike atomic systems  $(Z_p, e_1)_{f_1}$  and  $(Z_T, e_2)_{f_2}$ , respectively. Without resorting to some simplifying assumptions, the BCIS-3B method,

as a purely three-body theory, is not instantly usable for the four-particle process (63).

One such simplification of (63) is the frozen-core approximation in which the noncaptured, passive electron ( $e_2$ ) is assumed to occupy the same orbital before and after capture of the active electron ( $e_1$ ). Even this assumption can further be relaxed by eliminating altogether the explicit presence of the passive electron through the introduction of an effective hydrogenic model. In such a model, it is supposed that the hydrogenlike target  $(Z_T^{\text{eff}}, e_1)_{1s}$  could be a reasonable surrogate for describing the heliumlike atomic system  $(Z_T; e_1, e_2)_{1s^2}$ . Here,  $Z_T^{\text{eff}}$  is an effective charge of the target nucleus T. Physically, the effective hydrogenic model for (63) means that the passive electron  $e_2$  manifests its presence merely through a shielding effect by which the original nuclear charge  $Z_T$  is screened.

This is customarily done by using  $Z_T^{\text{eff}} = Z_T - Z_s$  in lieu of  $Z_T$ , where  $Z_s$  is the Slater screening constant charge. The extent of the Slater screening (i.e., the specific value of  $Z_s$ ) can be estimated by minimizing the expectation value of the total two-electron Hamiltonian (with the Coulomb potentials for the three pairs  $Z_T - e_1$ ,  $Z_T - e_2$ , and  $e_1 - e_2$ ) of a heliumlike atomic system in a set of any selected basis functions. For example, the simplest two-electron basis set would be a single element given by the product of the two ground-state hydrogenlike wave functions with the same effective nuclear charge  $Z_T^{\text{eff}}$ . Then, for any  $Z_T$  in the said Coulomb potentials from the total heliumlike Hamiltonian, its minimal expectation value would provide both  $Z_s$  and  $Z_T^{\text{eff}}$  as  $Z_s = \frac{5}{16}$  and  $Z_T^{\text{eff}} = Z_T - \frac{5}{16}$ , respectively. Thus, the effective hydrogenic model, which is used in many studies (including Ref. [40]), *de facto* replaces the original process (63) by its one-electron counterpart

$$Z_p + (Z_T^{\text{eff}}, e)_{1s} \rightarrow (Z_p, e)_{f_1} + Z_T^{\text{eff}}, \tag{64}$$

where the charge  $e_1$  of the only electron (electron 1) is relabeled as  $e$ . On the other hand, the charge  $e_2$  of the passive electron (electron 2) from the original process (63) with the target nuclear charge  $Z_T$  is present in (64) only by way of screening  $Z_T$  as  $Z_T^{\text{eff}} = Z_T - \frac{5}{16}$ . Overall, process (63) can be modeled by its hydrogenlike counterpart (64) through the replacement of  $(Z_T; e_1, e_2)_{1s^2}$  and  $(Z_T, e_2)_{f_2}$  by  $(Z_T^{\text{eff}}, e)_{1s}$  and  $Z_T^{\text{eff}}$ , respectively. This assumption reduces the BCIS-4B method for the four-body process (63) with a heliumlike target to the BCIS-3B method for an effective three-body process (64) with a hydrogenlike target. As such, the general expression for the  $T$  matrix in the BCIS-3B method for (7) applies also straight to (63) modeled by (64). Lastly, in order to connect the original and effective problems, it remains to double the cross sections for (64) to account for the presence of two electrons in the  $K$  shell of the original target  $(Z_T; e_1, e_2)_{1s^2}$  in (63). This is done because either of the two electrons ( $e_1$  or  $e_2$ ) from  $(Z_T; e_1, e_2)_{1s^2}$  in (63) can be captured with equal probability in the presently adopted spin-independent nonrelativistic formalism.

### III. RESULTS AND DISCUSSION

#### A. List of processes and inclusion of excited states

Cross sections are numerically computed by using the prior form of the BCIS-3B method for the following processes with single-electron capture from the target ground states

$$p + \text{H}(1s) \longrightarrow \text{H}(nlm) + p, \quad (65)$$

$$\alpha + \text{H}(1s) \longrightarrow \text{He}^+(nlm) + p, \quad (66)$$

$$p + \text{He}(1s^2) \longrightarrow \text{H}(nlm) + \text{He}^+(1s), \quad (67)$$

$$p + \text{H}(1s) \longrightarrow \text{H}(nl) + p, \quad (68)$$

$$\alpha + \text{H}(1s) \longrightarrow \text{He}^+(nl) + p, \quad (69)$$

$$p + \text{He}(1s^2) \longrightarrow \text{H}(nl) + \text{He}^+(1s), \quad (70)$$

$$p + \text{H}(1s) \longrightarrow \text{H}(n) + p, \quad (71)$$

$$\alpha + \text{H}(1s) \longrightarrow \text{He}^+(n) + p, \quad (72)$$

$$p + \text{He}(1s^2) \longrightarrow \text{H}(n) + \text{He}^+(1s), \quad (73)$$

$$p + \text{H}(1s) \longrightarrow \text{H}(\Sigma) + p, \quad (74)$$

$$\alpha + \text{H}(1s) \longrightarrow \text{He}^+(\Sigma) + p, \quad (75)$$

$$p + \text{He}(1s^2) \longrightarrow \text{H}(\Sigma) + \text{He}^+(1s), \quad (76)$$

where  $p$  and  $\alpha$  denote protons and alpha particles ( $\alpha \equiv \text{He}^{2+}$ ), respectively. Here and throughout this study, the analysis is limited to the initial ground state alone because in all the experimental data to be presently used, the targets H,  $\text{H}_2$ , He have been prepared in their ground states.

For process (67), no explicit reference is made to any two-electron transitions. In the literature, the final state of the noncaptured electron in the  $\text{He}^+$  ion from (67) is often set to

be the ground state ( $f_2 = 1s$ ). As stated earlier, even this is further simplified in our modeling of (67) by (64) through elimination of the explicit appearance of the noncaptured electron whose presence in both the initial and final channels is felt merely through the Slater screening  $Z_s$  of  $Z_T$ . For helium, we have  $Z_T = 2$ , so that  $Z_T^{\text{eff}} = 1.6875$ .

Total cross sections (state selective and state summed) in the BCIS-3B method have been obtained for all the processes (65)–(76). In particular for  $Z_T = 1$ , as mentioned, our general computer code can also provide directly differential cross sections without resorting to the cumbersome Fourier-Bessel numerical quadrature. This possibility is exploited here for computations of differential cross sections for (74).

#### B. Cross-section nomenclature and convergence of numerical quadratures

At every considered impact energy, in computations of state-summed total cross sections ( $Q_\Sigma$ ) for the genuinely hydrogenlike processes (74) and (75) as well as for (76) in the effective hydrogenic model (64) for (63) with  $Z_T^{\text{eff}} = 1.6875$ , all the excited states  $nlm$  have explicitly been included up to  $n = 4$ . Also, referring to differential cross sections for (74) the computations of  $(dQ/d\Omega)_\Sigma$  are performed by an explicit inclusion of the levels  $n \leq 4$  at  $E = 60$  keV as well as at 125 keV and  $n \leq 3$  at  $E = 5000$  keV. To account approximately for the final hydrogenlike states with  $n \geq 5$  for  $Q_\Sigma$  and  $(dQ/d\Omega)_\Sigma$ , use is made of the Oppenheimer  $n^{-3}$  scaling [15,27], borrowed from the first-order three-body OBK method

$$Q_\Sigma \approx Q_1 + Q_2 + Q_3 + 2.561Q_4, \quad (77)$$

$$\left(\frac{dQ}{d\Omega}\right)_\Sigma \approx \left(\frac{dQ}{d\Omega}\right)_1 + \left(\frac{dQ}{d\Omega}\right)_2 + \left(\frac{dQ}{d\Omega}\right)_3 + 2.561\left(\frac{dQ}{d\Omega}\right)_4, \quad (78)$$

respectively. As stated, (78) will be employed for  $(dQ/d\Omega)_\Sigma$  at  $E = 60$  and 125 keV. On the other hand, at  $E = 5000$  keV, the contributions from the states with  $n \geq 4$  will be approximated by the following simpler Oppenheimer formula:

$$\left(\frac{dQ}{d\Omega}\right)_\Sigma \approx \left(\frac{dQ}{d\Omega}\right)_1 + \left(\frac{dQ}{d\Omega}\right)_2 + 2.081\left(\frac{dQ}{d\Omega}\right)_3. \quad (79)$$

The reason for omitting the exact contribution from the  $n = 4$  shell in this computation is in relatively small differences already between the differential cross sections  $(dQ/d\Omega)_\Sigma$  for  $n \leq 2$  and  $n \leq 3$  as will be illustrated graphically. The theoretically predicted state-summed cross sections  $Q_\Sigma$  (total) and  $(dQ/d\Omega)_\Sigma$  (differential) are needed whenever no post-collisional information on any final bound states is provided by measurements.

The quantities  $Q_n$  (total) in (77) as well as  $(dQ/d\Omega)_n$  (differential) in (78) and (79) represent the cross sections for processes (71)–(73) with capture into the given  $n$  shell, summed over the subshells  $0 \leq l \leq n-1$  and  $-l \leq m \leq l$ , respectively. Likewise,  $Q_{nl}$  and  $(dQ/d\Omega)_{nl}$  are the corresponding cross sections for processes (68)–(70) with capture into the  $nl$  subshell, summed over the magnetic quantum numbers  $m \in [-l, +l]$ . All these quantities belong to the so-called partial cross sections, where the close ‘‘partial’’

emphasizes their explicit dependence on some of the three quantum numbers  $\{n, l, m\}$ . Then, such partial cross sections are written as

$$Q_n = \sum_{l=0}^{n-1} Q_{nl}, \quad Q_{nl} = \sum_{m=-l}^l Q_{nlm}, \quad (80)$$

$$\left(\frac{dQ}{d\Omega}\right)_n = \sum_{l=0}^{n-1} \left(\frac{dQ}{d\Omega}\right)_{nl}, \quad \left(\frac{dQ}{d\Omega}\right)_{nl} = \sum_{m=-l}^l \left(\frac{dQ}{d\Omega}\right)_{nlm}. \quad (81)$$

Further,  $Q_{nlm}$  and  $(dQ/d\Omega)_{nlm}$  are the total and differential cross sections, respectively, describing capture into the fixed individual  $nlm$  state in processes (65)–(67). As to measurements on single charge exchange, experimental data exist for processes (68)–(70), (71)–(73), as well as for (74)–(76) and these will be used for comparisons with the theoretical predictions. For brevity, in the ordinates of all the figures from our illustrations, we shall write  $Q$  or  $dQ/d\Omega$  with no subscripts. Nevertheless, with the provided captions and the labels near the curves in the figures, no confusion should arise.

The Gauss-Legendre quadrature order NGL (the number of the integration points) is varied between 368 and 1616 per each of the three integration axes to achieve a satisfactory convergence for total cross sections, as well as for the differential cross sections at intermediate energies of 60 and 125 keV. For each result, convergence to at least two decimal places has been achieved. For differential cross sections at  $E = 5$  MeV, a larger number of integration points were required (up to NGL = 4000 for  $n = 3$ ). This was necessary in order to stabilize the results from the integrands whose high oscillations are enhanced at increased impact energies. All the numerical quadratures in the differential and total cross sections (state selective and state summed) have been performed using the same fixed-order NGL per integration axis directly over the entire integration limits (i.e., with no splitting of the integration intervals into a number of smaller subintervals).

### C. Electron capture from H(1s) by protons into any excited states of hydrogen H( $nlm$ )

The numerical values of the state-selective ( $Q_{nlm}$ ,  $Q_{nl}$ ,  $Q_n$ ) and state-summed ( $Q_\Sigma$ ) total cross sections in the BCIS-3B method for processes (65), (68), (71), and (74), respectively, from our computations within the energy range  $10 \text{ keV} \leq E \leq 1000 \text{ keV}$  are presented in Table I. To complement this information, our results are also shown in Figs. 1–3. Both tabular and graphical presentations are deemed useful for enabling the readily accessible, parallel displays and analysis.

The cross sections  $Q_{1s}$ ,  $Q_{2s}$ , and  $Q_{2p}$  for capture into the  $1s$ ,  $2s$ , and  $2p$  states for process (68) are in Fig. 1. Therein, Fig. 1(a) is for  $Q_{1s}$  and  $Q_{2s}$ , whereas Fig. 1(b) is for  $Q_{2p}$ . Further,  $Q_{3s}$ ,  $Q_{3p}$ , and  $Q_{3d}$  for capture into  $3s$ ,  $3p$ , and  $3d$  states are in Fig. 2. Moreover,  $Q_{4s}$ ,  $Q_{4p}$ ,  $Q_{4d}$ , and  $Q_{4f}$  for capture into the  $4s$ ,  $4p$ ,  $4d$ , and  $4f$  states are in Fig. 3. The adequacy of these state-selective cross sections  $Q_{nl}$  is assessed in relation to the available experimental data [76–88]. Importantly, various experimental data from Figs. 1–3 for capture

into the spherically symmetric states ( $2s$ ,  $3s$ ,  $4s$ ) are in very good mutual accord. The experimental data measured with a molecular hydrogen target  $\text{H}_2$  (cross sections per molecule) are transformed to their counterparts corresponding to an atomic hydrogen target  $\text{H}$  (cross sections per atom) following Ref. [89] while using the measured energy-dependent cross-section ratios  $Q_{\text{H}_2}/Q_{\text{H}}$ .

The present results from Figs. 1–3 for capture into the  $2s$ ,  $3s$ , and  $4s$  states exhibit excellent agreement with the experimental data throughout the displayed intermediate energy range (10–300 keV). This is all the more remarkable given that the BCIS-3B method is, by construction, a high-energy theory. Generally, some discrepancies between the BCIS-3B method and measurements are, therefore, expected at intermediate energies. However, there are none for capture into the  $2s$ ,  $3s$ , and  $4s$  states (Figs. 1–3). For example, agreement between theory and experiments is excellent even down to 10 keV for capture into the  $3s$  state (Fig. 2).

Also of interest is to compare our findings with those from other theoretical methods. To assess the lowest-energy validity limit of the perturbative formalisms, such as the BCIS-3B approximation, it is useful to recall the results from some nonperturbative methods [7–9] because these usually provide reliable cross sections especially at lower-to-intermediate energies. This is exemplified in Fig. 1 for electron capture in the process  $\text{H}^+ + \text{H}(1s) \rightarrow \text{H}(nl) + \text{H}^+$  with  $nl = 1s$  as well as  $nl = 2s$  on Fig. 1(a) and  $nl = 2p$  on Fig. 1(b). Here, the considered nonperturbative theories are the Sturmian-state expansion (SSE) [7], the time-dependent Schrödinger equation (TDSE) [8], and the semiclassical convergent close-coupling (SC-CCC) methods [9]. It is deemed useful, as well, to refer here to the pertinent results from one of the most important high-energy perturbative theories, the CDW-3B method ( $nl = 1s$  [18],  $nl = 2s$ ,  $2p$  [1,89]).

Remarkably good agreement is seen for resonant capture ( $nl = 1s$ ) in Fig. 1(a) when juxtaposing the perturbative BCIS-3B and CDW-3B methods to the nonperturbative SSE and TDSE methods. The BCIS-3B and CDW-3B methods closely follow each other at  $40 \leq E \leq 1000 \text{ keV}$ . Moreover,  $Q_{1s}^{(\text{SSE})}$  and  $Q_{1s}^{(\text{TDSE})}$  are also highly concordant at the energies of overlap  $E \leq 200 \text{ keV}$  (the latter cross sections extend to 630 keV).

Figure 1(a) deals with nonresonant capture ( $nl = 2s$ ), as well. In this case, advantageously, several sets of measured cross sections are available (albeit only at moderately intermediate energies,  $E \leq 180 \text{ keV}$ ). Here, excellent agreement is recorded between the BCIS-3B method and the experimental data at  $20 \leq E \leq 150 \text{ keV}$ . It is also clear that the BCIS-3B and CDW-3B methods are very coherent with each other at  $50 \leq E \leq 1000 \text{ keV}$ . In Fig. 1(a), in addition to the SSE and TDSE methods, we refer to the SC-CCC method, as well. At  $20 \leq E \leq 200 \text{ keV}$ , the BCIS-3B and SSE methods are in excellent agreement. Moreover, the BCIS-3B method agrees very well with the SC-CCC and TDSE methods at  $20 \leq E \leq 170 \text{ keV}$  and  $40 \leq E \leq 170 \text{ keV}$ , respectively. At  $E \leq 40 \text{ keV}$ , the predictions with the TDSE method are below those due to the BCIS-3B method by at most a factor of 1.3.

Uncustomarily, at  $E > 170 \text{ keV}$ , the cross sections by the TDSE method abruptly fall off exhibiting a large departure from the other theoretical results. For example, at 300 keV,

TABLE I. State-selective total cross sections (in  $10^{-16}$  cm<sup>2</sup>) for processes (65), (68), and (74) as a function of impact energy  $E$  (keV) of protons for electron capture from H(1s) into the final bound states of atomic hydrogen with  $n \leq 4$ . The column labeled by  $nlm$  refers to the state-selective (or partial) cross sections  $Q_{nlm}$  and  $Q_{nl}$  for (65) and (68), respectively. The row denoted by  $\Sigma$  represents the cross sections  $Q_{\Sigma}$ , summed over all the final bound states of the H( $nlm$ ) atom, by using Eq. (77). Notation  $X[Z]$  implies  $X \times 10^Z$ .

$nlm \setminus E$ (keV)	10	20	30	50	80	100
100	1.28[+1]	4.97	2.24	6.34[-1]	1.52[-1]	7.05[-2]
200	2.04[-1]	3.78[-1]	2.82[-1]	1.10[-1]	2.87[-2]	1.33[-2]
210	1.02[-1]	2.05[-1]	1.52[-1]	5.28[-2]	1.13[-2]	4.61[-3]
211	1.66[-2]	3.60[-2]	2.44[-2]	7.43[-3]	1.41[-3]	5.49[-4]
2p	1.35[-1]	2.77[-1]	2.01[-1]	6.76[-2]	1.41[-2]	5.71[-3]
300	3.41[-2]	8.89[-2]	7.74[-2]	3.35[-2]	9.10[-3]	4.24[-3]
310	1.92[-2]	5.05[-2]	4.52[-2]	1.81[-2]	4.11[-3]	1.70[-3]
311	2.43[-3]	8.46[-3]	6.97[-3]	2.44[-3]	4.95[-4]	1.95[-4]
3p	2.40[-2]	6.75[-2]	5.92[-2]	2.30[-2]	5.10[-3]	2.09[-3]
320	1.58[-3]	4.16[-3]	3.61[-3]	1.29[-3]	2.40[-4]	8.84[-5]
321	3.82[-4]	1.53[-3]	1.30[-3]	4.17[-4]	7.01[-5]	2.46[-5]
322	4.79[-5]	1.89[-4]	1.49[-4]	4.42[-5]	6.96[-6]	2.37[-6]
3d	2.44[-3]	7.60[-3]	6.50[-3]	2.21[-3]	3.94[-4]	1.42[-4]
400	1.18[-2]	3.42[-2]	3.16[-2]	1.42[-2]	3.93[-3]	1.83[-3]
410	7.00[-3]	1.97[-2]	1.88[-2]	7.98[-3]	1.85[-3]	7.69[-4]
411	8.00[-4]	3.24[-3]	2.86[-3]	1.06[-3]	2.20[-4]	8.72[-5]
4p	8.60[-3]	2.62[-2]	2.46[-2]	1.01[-2]	2.29[-3]	9.43[-4]
420	7.67[-4]	2.11[-3]	1.96[-3]	7.47[-4]	1.44[-4]	5.33[-5]
421	1.66[-4]	7.54[-4]	6.97[-4]	2.39[-4]	4.15[-5]	1.47[-5]
422	1.96[-5]	9.27[-5]	7.89[-5]	2.50[-5]	4.07[-6]	1.40[-6]
4d	1.14[-3]	3.81[-3]	3.52[-3]	1.28[-3]	2.35[-4]	8.55[-5]
430	2.23[-5]	6.82[-5]	6.12[-5]	2.03[-5]	3.18[-6]	1.04[-6]
431	6.83[-6]	3.27[-5]	3.10[-5]	9.84[-6]	1.44[-6]	4.55[-7]
432	1.39[-6]	8.27[-6]	7.29[-6]	2.12[-6]	2.85[-7]	8.72[-8]
433	1.51[-7]	8.14[-7]	6.73[-7]	1.85[-7]	2.40[-8]	7.21[-9]
4f	3.90[-5]	1.52[-4]	1.39[-4]	4.46[-5]	6.67[-6]	2.14[-6]
$\Sigma$	1.32[+1]	5.96	3.02	9.36[-1]	2.26[-1]	1.03[-1]
$nlm \setminus E$ (keV)	150	200	300	500	800	1000
100	1.51[-2]	4.56[-3]	7.37[-4]	6.17[-5]	5.47[-6]	1.67[-6]
200	2.74[-3]	7.88[-4]	1.19[-4]	9.16[-6]	7.68[-7]	2.30[-7]
210	7.28[-4]	1.70[-4]	1.85[-5]	9.20[-7]	5.00[-8]	1.21[-8]
211	8.00[-5]	1.78[-5]	1.84[-6]	8.80[-8]	4.75[-9]	1.15[-9]
2p	8.88[-4]	2.06[-4]	2.22[-5]	1.10[-6]	5.95[-8]	1.44[-8]
300	8.68[-4]	2.48[-4]	3.68[-5]	2.80[-6]	2.32[-7]	6.93[-8]
310	2.70[-4]	6.27[-5]	6.78[-6]	3.33[-7]	1.79[-8]	4.31[-9]
311	2.88[-5]	6.40[-6]	6.60[-7]	3.14[-8]	1.69[-9]	4.09[-10]
3p	3.27[-4]	7.55[-5]	8.10[-6]	3.95[-7]	2.13[-8]	5.13[-9]
320	1.09[-5]	2.08[-6]	1.65[-7]	5.27[-9]	1.86[-10]	3.65[-11]
321	2.81[-6]	5.10[-7]	3.82[-8]	1.16[-9]	4.01[-11]	7.80[-12]
322	2.59[-7]	4.54[-8]	3.29[-9]	9.78[-11]	3.38[-12]	6.63[-13]
3d	1.71[-5]	3.19[-6]	2.48[-7]	7.80[-9]	2.73[-10]	5.35[-11]
400	3.75[-4]	1.07[-4]	1.58[-5]	1.19[-6]	9.88[-8]	2.94[-8]
410	1.22[-4]	2.84[-5]	3.06[-6]	1.49[-7]	8.02[-9]	1.93[-9]
411	1.29[-5]	2.87[-6]	2.96[-7]	1.40[-8]	7.53[-10]	1.82[-10]
4p	1.48[-4]	3.41[-5]	3.65[-6]	1.78[-7]	9.52[-9]	2.29[-9]
420	6.64[-6]	1.26[-6]	1.00[-7]	3.19[-9]	1.12[-10]	2.20[-11]
421	1.69[-6]	3.07[-7]	2.30[-8]	7.02[-10]	2.41[-11]	4.69[-12]
422	1.54[-7]	1.97[-8]	1.97[-9]	5.88[-11]	2.03[-12]	3.98[-13]
4d	1.03[-5]	1.93[-6]	1.50[-7]	4.71[-9]	1.65[-10]	3.22[-11]
430	1.00[-7]	1.55[-8]	8.92[-10]	1.84[-11]	4.24[-13]	6.74[-14]
431	4.13[-8]	6.17[-9]	3.41[-10]	6.78[-12]	1.53[-13]	2.42[-14]
432	7.43[-9]	1.07[-9]	5.60[-11]	1.06[-12]	2.33[-14]	3.66[-15]
433	5.94[-10]	8.33[-11]	4.27[-12]	7.97[-14]	1.76[-15]	2.80[-16]
4f	1.99[-7]	3.02[-8]	1.69[-9]	3.42[-11]	7.81[-13]	1.24[-13]
$\Sigma$	2.13[-2]	6.24[-3]	9.73[-4]	7.86[-5]	6.83[-6]	2.07[-6]

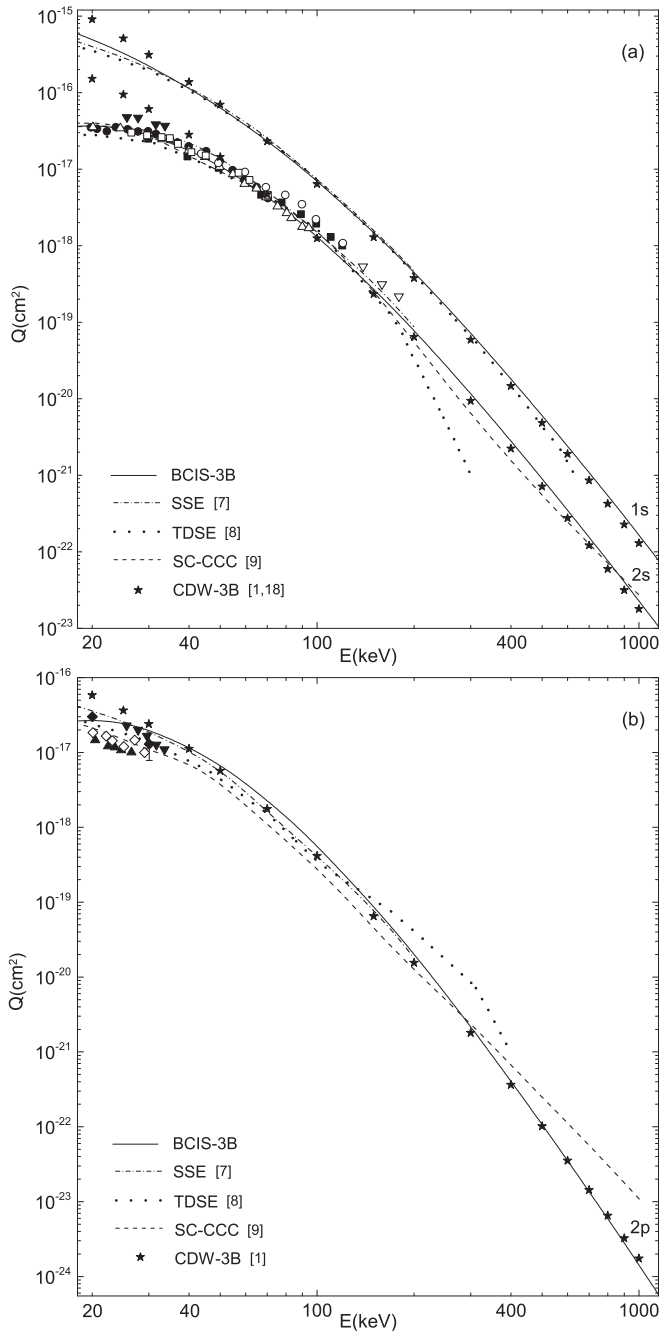


FIG. 1. State-selective total cross sections  $Q_{1s}$ ,  $Q_{2s}$ , and  $Q_{2p}$  in  $\text{cm}^2$  as a function of impact energies  $E$  (keV) for electron capture by protons from  $\text{H}(1s)$ , as per process (68). The solid curves are the present results from the BCIS-3B method, whereas the star symbols ( $\star$ ) are for  $Q_{nl}$  from the CDW-3B method [1,18]. The dotted-dashed, dotted, and dashed curves are from the SSE [7], TDSE [8], and SC-CCC methods [9], respectively. Experimental data with atomic hydrogen targets:  $\circ$  ( $Q_{2s}$ ) Ryding *et al.* [76],  $\bullet$  ( $Q_{2s}$ ) Bayfield [77],  $\triangle$  ( $Q_{2s}$ ) Morgan *et al.* [78],  $\blacklozenge$  ( $Q_{2p}$ ) Stebbings *et al.* [79],  $\blacktriangle$  ( $Q_{2p}$ ) Morgan *et al.* [80],  $\diamond$  ( $Q_{2p}$ ) Kondow *et al.* [81]. Experimental data with molecular hydrogen targets (converted to atomic hydrogen targets following Ref. [89]):  $\nabla$  ( $Q_{2s}$ ) Ryding *et al.* [76],  $\blacktriangledown$  ( $Q_{2s}$ ,  $Q_{2p}$ ) Andreev *et al.* [82],  $\square$  ( $Q_{2s}$ ) Bayfield [83],  $\blacksquare$  ( $Q_{2s}$ ) Hughes *et al.* [84].

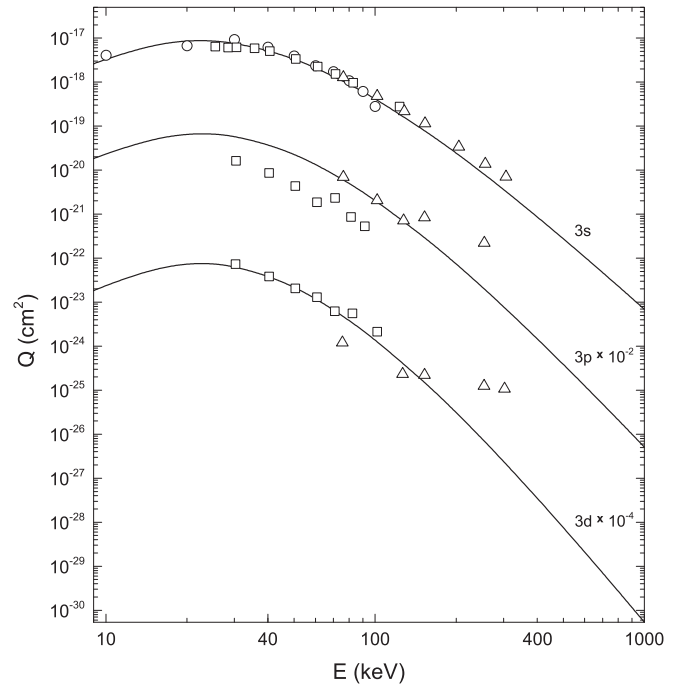


FIG. 2. State-selective total cross sections  $Q_{3s}$ ,  $Q_{3p}$ , and  $Q_{3d}$  in  $\text{cm}^2$  as a function of impact energies  $E$  (keV) for electron capture by protons from  $\text{H}(1s)$ , as per process (68). The curves are the present results from the BCIS-3B method. Experimental data with atomic hydrogen targets:  $\circ$  ( $Q_{3s}$ ) Hughes *et al.* [85]. Experimental data with molecular hydrogen targets (converted to atomic hydrogen targets following Ref. [89]):  $\square$  ( $Q_{3s}$ ,  $Q_{3p}$ ,  $Q_{3d}$ ) Hughes *et al.* [87],  $\triangle$  ( $Q_{3s}$ ,  $Q_{3p}$ ,  $Q_{3d}$ ) Ford and Thomas [88]. Both the theoretical and experimental results are divided by a factor:  $Q_{3p}$  by  $10^2$  and  $Q_{3d}$  by  $10^4$ .

the TDSE method underestimates the BCIS-3B and SC-CCC methods by a factor of 7 and 4, respectively. Although above  $E > 170$  keV to about 850 keV,  $Q_{2s}^{(\text{SC-CCC})}$  lie below  $Q_{2s}^{(\text{BCIS-3B})}$ , the shapes of the corresponding solid and dashed curves are reasonably concordant. Unfortunately, for quantitative testings of the theories against experiments, there are no measured cross sections  $Q_{2s}$  above 200 keV. Further, from 850 to 1000 keV, a reversed pattern exists for formation of  $\text{H}(2s)$ , in which case  $Q_{2s}^{(\text{SC-CCC})}$  begins to overestimate  $Q_{2s}^{(\text{BCIS-3B})}$ , albeit very slightly.

Regarding capture into the  $2p$  state, Fig. 1(b) shows that at  $30 \leq E \leq 1000$  keV, the BCIS-3B and CDW-3B methods are in a remarkably good agreement. Also, reasonable-to-very good agreement is observed at  $20 \leq E \leq 200$  keV between the BCIS-3B and SSE methods. Below 130 keV,  $Q_{2p}^{(\text{BCIS-3B})}$  lies above  $Q_{2p}^{(\text{TDSE})}$  and  $Q_{2p}^{(\text{SC-CCC})}$ . Conversely,  $Q_{2p}^{(\text{TDSE})}$  and  $Q_{2p}^{(\text{SC-CCC})}$  are above  $Q_{2p}^{(\text{BCIS-3B})}$  at  $E > 130$  keV and  $E > 300$  keV, respectively. Here,  $Q_{2p}^{(\text{TDSE})}$  exhibits an unusual sudden slope change at 300 keV and from thereon shows a fast decline with increased energy. This experimentally unobserved pattern runs contrary to the smoothly behaving cross sections  $Q_{2p}^{(\text{BCIS-3B})}$ ,  $Q_{2p}^{(\text{CDW-3B})}$ , and  $Q_{2p}^{(\text{SC-CCC})}$  at higher energies. At, e.g., 200 keV,  $Q_{2p}^{(\text{TDSE})}$  overestimates  $Q_{2p}^{(\text{SSE})}$  by a factor of 2. The TDSE and SC-CCC methods are in good agreement at  $20 \leq E \leq 100$  keV, but differ very significantly at higher energies. For example at

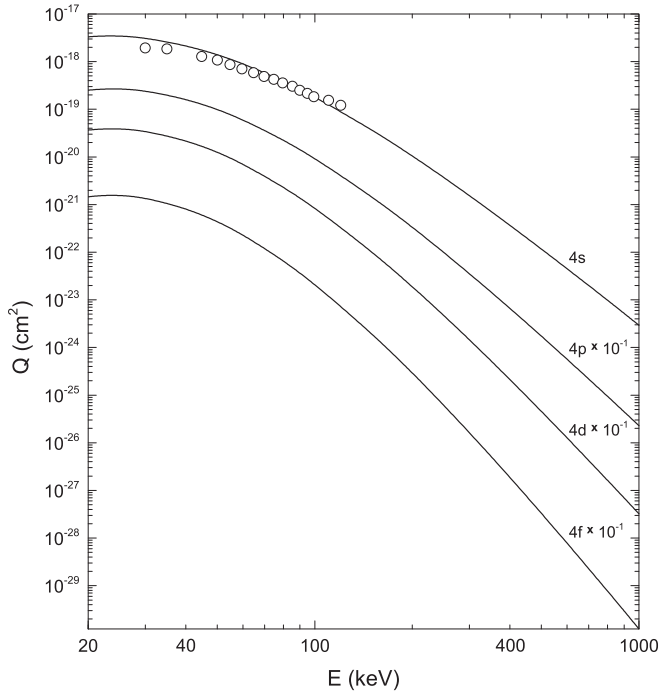


FIG. 3. State-selective total cross sections  $Q_{4s}$ ,  $Q_{4p}$ ,  $Q_{4d}$ , and  $Q_{4f}$  in  $\text{cm}^2$  as a function of impact energies  $E$  (keV) for electron capture by protons from  $\text{H}(1s)$ , as per process (68). The curves are the present results from the BCIS-3B method. Experimental data with molecular hydrogen targets (converted to atomic hydrogen targets following Ref. [89]):  $\circ$  ( $Q_{4s}$ ) Hughes *et al.* [86]. The theoretical results for  $Q_{4p}$ ,  $Q_{4d}$ , and  $Q_{4f}$  are divided by 10.

280 keV, it is seen that  $Q_{2p}^{(\text{TDSE})} \approx 3.5Q_{2p}^{(\text{SC-CCC})}$ , while at this same energy we have  $Q_{2p}^{(\text{SC-CCC})} \approx Q_{2p}^{(\text{BCIS-3B})}$ .

From 20 to 200 keV, we note that  $Q_{2p}^{(\text{SC-CCC})} < Q_{2p}^{(\text{BCIS-3B})}$  and the difference between these two cross sections is within a factor of 2. On the other hand, a more favorable agreement at the same energies ( $20 \leq E \leq 200$  keV) is seen between the BCIS-3B and SSE methods. Above 280 keV, a strong pattern reversal occurs between the SC-CCC and BCIS-3B methods  $Q_{2p}^{(\text{SC-CCC})} > Q_{2p}^{(\text{BCIS-3B})}$ , such that at, e.g., 1000 keV, there is factor of 10 difference  $Q_{2p}^{(\text{SC-CCC})} \approx 10Q_{2p}^{(\text{BCIS-3B})}$ . This should be compared to a near coincidence of  $Q_{2p}^{(\text{SC-CCC})}$  and  $Q_{2p}^{(\text{CDW-3B})}$ . In fact, it is mainly the lack of experimental data on  $Q_{2p}$  above 35 keV, coupled with an order-of-magnitude discrepancy between the SC-CCC and BCIS-3B methods at high energies that motivates bringing the CDW-3B method into the presentation. For the other electronic transitions, we shall not pursue any further with the presentations of the results from the CDW-3B method, as the interested reader can consult, e.g., Refs. [1,89].

At the highest displayed energies in Fig. 1(b), the discrepancy between  $Q_{2p}^{(\text{BCIS-3B})}$  and  $Q_{2p}^{(\text{SC-CCC})}$ , toward the tails of the two curves (above 300 keV), is more pronounced than that in Fig. 1(a) between  $Q_{2s}^{(\text{BCIS-3B})}$  and  $Q_{2s}^{(\text{SC-CCC})}$  (above 850 keV). This implies that the neglected ionization channel in the SC-CCC method influences more significantly capture to the  $2p$  than to the  $2s$  subshells of the  $n = 2$  level in atomic hydrogen. Ionization dominates over capture at higher energies where

it is important to include electron continuum states as an intermediate channel prior to capture. It is such an intermediate ionization effect which places the BCIS-3B method into the category of the second-order perturbative theories. This is contrary to first-order theories such as the CB1-3B method where the purely electronic continuum intermediate states are absent from the onset.

As to the existing experimental data for  $Q_{2p}$ , they are scarce, unfortunately. Moreover, they do not extend to energies above 35 keV. Further, it is seen in Fig. 1(b) that the measured  $Q_{2p}$  from Refs. [79,81] are not fully concordant with each other. A similar discrepancy within a factor of 2 also exists between the measured  $Q_{2p}$  from Refs. [80,82]. For example, one finds that  $1.99 \leq Q_{2p}^{\text{Ref.}[82]} / Q_{2p}^{\text{Ref.}[81]} \leq 2.1$  and  $1.4 \leq Q_{2p}^{\text{Ref.}[79]} / Q_{2p}^{\text{Ref.}[81]} \leq 1.9$ . It is clear that both  $Q_{2p}^{(\text{BCIS-3B})}$  and  $Q_{2p}^{(\text{SSE})}$  are in very good agreement with the experimental data from Refs. [79,82], while showing an overestimation of the measured cross sections from Refs. [80,81]. On the other hand,  $Q_{2p}^{(\text{SC-CCC})}$  agrees very well with the measured findings from Refs. [80,81], but underestimates the experimental data from Refs. [79,82]. At these limited sets of the existing experimental data, the cross sections  $Q_{2p}^{(\text{TDSE})}$  are in-between  $Q_{2p}^{(\text{BCIS-3B})}$  and  $Q_{2p}^{(\text{SC-CCC})}$ , with the TDSE method being closer to the SC-CCC than to the BCIS-3B or SSE methods.

Figure 2 deals with capture into the  $n = 3$  level with the three pertinent subshells  $3s$ ,  $3p$ , and  $3d$ . Therein, the three sets of measurements [85,87,88] for  $Q_{3s}$  are in very good agreement. These measured cross sections are excellently reproduced by the BCIS-3B method at all energies, 10–300 keV. As to the experimental data for  $Q_{3l}$  from the same Refs. [87,88], they are seen to be scattered for both  $l = 1$  and 2. The BCIS-3B method for  $Q_{3p}$  excellently coheres with the measured cross sections from Ref. [88] at 75–125 keV, but underestimates them above 125 keV. However, the trend of the two measured cross sections at 150 and 250 keV [88] does not follow the data at 75–125 keV from the same experiment. The experimental data for  $Q_{3p}$  from Ref. [87] are overestimated by the BCIS-3B method at 30–100 keV. Similarly, the measured cross sections  $Q_{3p}$  from Ref. [87] underestimate those from experiments in Ref. [88] at the overlapped energies (70–100 keV). The results for  $Q_{3d}$  by the BCIS-3B method are in excellent agreement with the experimental data from Ref. [87] at all energies (30–100 keV). Moreover,  $Q_{3d}$  agrees very well with the measured cross sections from Ref. [88] at  $E \leq 150$  keV. Also seen in Fig. 2 is that, above 150 keV, the BCIS-3B method for capture into the  $3d$  state underestimates the just mentioned experimental data [88]. However, these latter recorded data for  $Q_{3d}$  at 250 and 300 keV are clearly out of line relative to those at 75–150 keV from the same measurement [88]. New measurements on  $Q_{3p}$  and  $Q_{3d}$  would be desirable to settle the issue of the existing disparity in the two measurements [87,88] and to help solidify the assessment of the performance of the theory for capture into the  $3p$  and  $3d$  states.

Cross sections  $Q_{4s}$ ,  $Q_{4p}$ ,  $Q_{4d}$ , and  $Q_{4f}$  from the BCIS-3B method are given in Fig. 3. Comparison of the theory and measurement deals with  $Q_{4s}$  alone since there are no experimental data for  $Q_{4l}$  ( $l = 1, 2, 3$ ) at intermediate and high energies. It is observed in this figure that the BCIS-3B method for  $Q_{4s}$

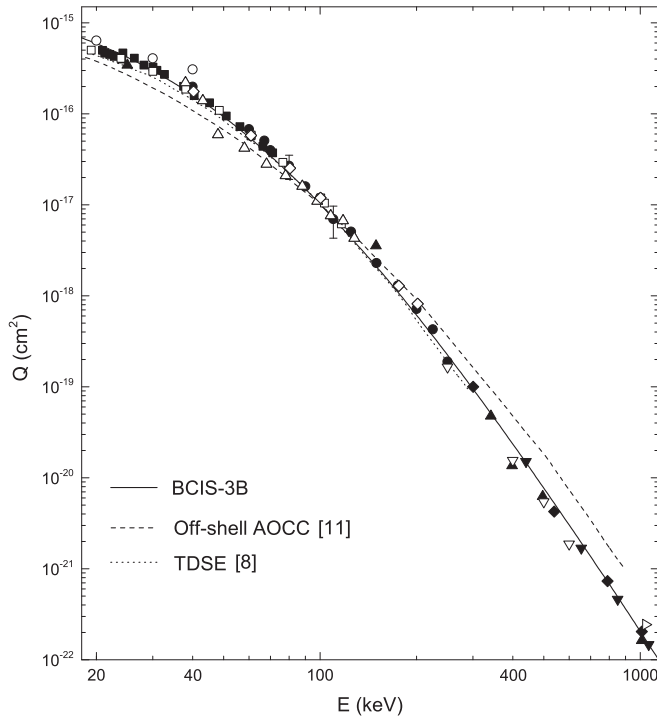


FIG. 4. State-summed total cross sections  $Q_{\Sigma}$  (cm<sup>2</sup>) as a function of impact energies  $E$  (keV) for electron capture into all the final bound states  $H(\Sigma)$  from the ground state of atomic hydrogen by protons. Theories: various curves. The solid curve: the present result  $Q_{\Sigma}$  from the BCIS-3B method with  $Q_{\Sigma} \simeq Q_1 + Q_2 + Q_3 + 2.561Q_4$  using (77); the dotted curve:  $Q_{\Sigma}$  from the TDSE method [8] with  $Q_{\Sigma} \simeq Q_1 + 1.616Q_2$ ; and the dashed curve:  $Q_1 \equiv Q_{1s}$  from the off-shell AOCC method [11]. The cross sections  $Q_{\Sigma} \simeq Q_1 + 1.616Q_2$  from the SSE method [7] (not plotted) are very close to  $Q_{\Sigma}$  from the TDSE method [8]. Experimental data with atomic hydrogen targets:  $\circ$  Fite *et al.* [90],  $\square$  McClure [91],  $\triangle$  Gilbody and Ryding [92],  $\bullet$  Wittkower *et al.* [93],  $\blacksquare$  Bayfield [77],  $\nabla$  Hvelplund and Andersen [94]. Experimental data with molecular hydrogen targets (converted to atomic hydrogen targets following Ref. [89]):  $\diamond$  Stier and Barnett [95],  $\blacktriangle$  Barnett and Reynolds [96],  $\blacktriangledown$  Welsh *et al.* [97],  $\triangleright$  Schryber [98],  $\blacklozenge$  Toburen *et al.* [99].

is able to excellently reproduce the corresponding measured cross sections from Ref. [86] at all the energies (30–125 keV). For completion, despite the said lack of measurements on  $Q_{4p}$ ,  $Q_{4d}$ , and  $Q_{4f}$ , these cross sections are also plotted on Fig. 3.

The total cross sections  $Q_{\Sigma}^{(\text{BCIS-3B})}$  from the BCIS-3B method are displayed in Fig. 4 as the solid curve. These cross sections are summed over all the final bound states by means of the Oppenheimer scaling rule (77). In Fig. 4, the experimental data from the great majority of the existing measurements [90–99] appear to be in very good mutual accord. Here too, as was the case with the state-selective (state-resolved) cross sections, experimental data measured on molecular hydrogen targets are converted to the corresponding atomic hydrogen targets following Ref. [89]. As is clear from this figure, the BCIS-3B method is in excellent agreement with all the measured cross sections throughout the wide energy range from 20 to 1000 keV, within which the cross sections vary by some seven orders of magnitude. Also plotted in Fig. 4

are the cross sections  $Q_{\Sigma}^{(\text{TDSE})}$  [8] and those from the off-shell atomic-orbital close-coupling (AOCC) method [11]. Cross sections  $Q_{nl}^{(\text{TDSE})}$  are available up to 600, 300, and 400 keV for  $nl = 1s, 2s$ , and  $2p$ , respectively [8]. These provide  $Q_{\Sigma}^{(\text{TDSE})}$  up to 300 keV using the usual Oppenheimer-scaled formula  $Q_{\Sigma}^{(\text{TDSE})} = Q_{1s}^{(\text{TDSE})} + 1.616[Q_{2s}^{(\text{TDSE})} + Q_{2p}^{(\text{TDSE})}]$ . It is noted that  $Q_{\Sigma}^{(\text{BCIS-3B})}$  and  $Q_{\Sigma}^{(\text{TDSE})}$  are in perfect agreement at  $30 \leq E \leq 300$  keV. Very good agreement exists as well between the BCIS-3B and the off-shell AOCC method at  $20 \leq E \leq 200$  keV. Above 200 keV, where intermediate ionization channels become dominant, the off-shell AOCC method overestimates the experimental data. Conceivably, that inclusion of coupling to ionization channels would bring the cross sections from the off-shell AOCC method closer to the measured data at  $E > 200$  keV, as indeed was the expectation expressed in Ref. [11].

We shall now analyze theoretical (present, Ref. [11]) and measured angular distributions [100–102] of scattered projectiles (differential cross sections) that are shown in Figs. 5–7. Specifically, Figs. 5 and 6 are for the intermediate energies  $E_{\text{cm}} = 60$  and 125 keV, respectively, whereas Fig. 7 deals with a high impact energy  $E_{\text{lab}} = 5$  MeV. To avoid clutter, the state-selective cross sections  $(dQ/d\Omega)_n$  for  $1 \leq n \leq 4$  and the state-summed cross sections  $(dQ/d\Omega)_{\Sigma}$  are shown on two separate panels, (a) and (b), respectively, in Figs. 5 and 6. On the other hand, at 5 MeV in Fig. 7, all the curves are sufficiently transparent when plotting together  $(dQ/d\Omega)_n$  for  $1 \leq n \leq 3$  and  $(dQ/d\Omega)_{\Sigma}$ .

Figures 5(a) and 6(a) show that the dominant contribution to  $(dQ/d\Omega)_{\Sigma}$  comes from  $(dQ/d\Omega)_1$ . Therein, all the curves for  $(dQ/d\Omega)_n$  with  $1 \leq n \leq 4$  and  $(dQ/d\Omega)_1$  have similar shapes with no minima. As seen in Figs. 5(b) (60 keV) and 6(b) (125 keV), the BCIS-3B method is in good agreement with the experimental data [100,101]. Moreover, in these figures, the BCIS-3B method and experimental data exhibit similar curvature changes near 1 mrad. In the BCIS-3B method, this is a consequence of a competition between two different mechanisms, one stemming from electronic and the other from nuclear motions. The electron-nucleus interaction underlies the former mechanism, whereas the basis of the latter mechanism is the nucleus-nucleus elastic Rutherford scattering. The electron-nucleus component dominates at smaller angles (near the forward cone, i.e., close to  $\theta = 0$ ). Its prominent signature for decreasing  $\theta$  is a sharp rise of the differential cross section which eventually culminates as the forward peak ( $\theta \approx 0$ ). The nucleus-nucleus Rutherford component is negligible in the vicinity of the forward cone, but prevails at larger  $\theta$ . In the Rutherford mechanism, the differential cross sections are not peaked. Quite the contrary, the associated curve has an extended tail as a function of  $\theta$ . Since these two component curves possess different slopes (not shown), their interference yields the curvature change in the composite result, displayed in the BCIS-3B method by the solid curves on panels (a) and (b). Such features persist at both 60 keV (Fig. 5) and 125 keV (Fig. 6).

Also depicted on Figs. 5(b) and 6(b) are the differential cross sections from the on- and off-shell AOCC methods [11] as the dashed and dotted curves, respectively. It is observed that the BCIS-3B and off-shell AOCC methods agree well with each other as well as with the experimental data

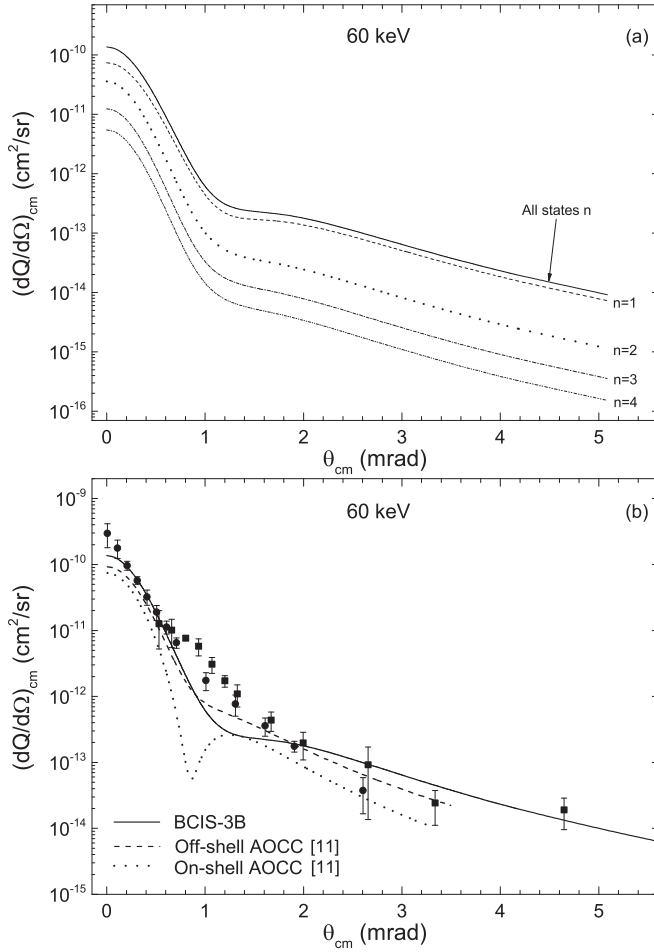


FIG. 5. Differential cross sections  $(dQ/d\Omega)_n$  and  $(dQ/d\Omega)_\Sigma$  (in  $\text{cm}^2/\text{sr}$ ) as a function of scattering angle  $\theta$  (in mrad) at the impact energy  $E = 60$  keV for electron capture by protons from  $\text{H}(1s)$  into the state-selective states of  $\text{H}(n)$  and into all the states of  $\text{H}(\Sigma)$ . Both the cross sections and the scattering angles are in the center-of-mass system. (a) Only the present results from the BCIS-3B method for  $(dQ/d\Omega)_n$  with  $1 \leq n \leq 4$  and  $(dQ/d\Omega)_\Sigma = (dQ/d\Omega)_1 + (dQ/d\Omega)_2 + (dQ/d\Omega)_3 + 2.561(dQ/d\Omega)_4$ . (b) The solid curve (present) from the BCIS-3B method for  $(dQ/d\Omega)_\Sigma$ , whereas the dashed and dotted curves are from the off- and on-shell AOCC methods [11], respectively. Experimental data with atomic hydrogen targets: ● Martin *et al.* [100], ■ Park [101].

[100,101]. On the other hand, the dotted curves for the on-shell AOCC method have minima at 0.9 and 0.7 mrad at 60 keV (Fig. 5) and 125 keV (Fig. 6). There are no minima in the experimental data nor in the BCIS-3B and the off-shell AOCC methods.

For proton-hydrogen charge exchange, the CB1-3B, BCIS-3B, as well as the AOCC methods share the same potential comprised of the nucleus-nucleus and electron-projectile interactions ( $1/R - 1/s$ ). It is well known that an infinitely deep minimum (a dip) always appears in  $(dQ/d\Omega)_{nlm}^{(\text{CB1-3B})}$  for any fixed triple  $nlm$ , as illustrated in Ref. [26] for  $1 \leq n \leq 9$ . This is due to a nearly complete vanishing of the potential  $1/R - 1/s$  at the so-called dark angle (da),  $\theta_{da}$ , located at 1.1, 0.9, and 0.7 mrad for 25, 60, and 125 keV, respectively (the larger the impact energy, the smaller the dark angle)

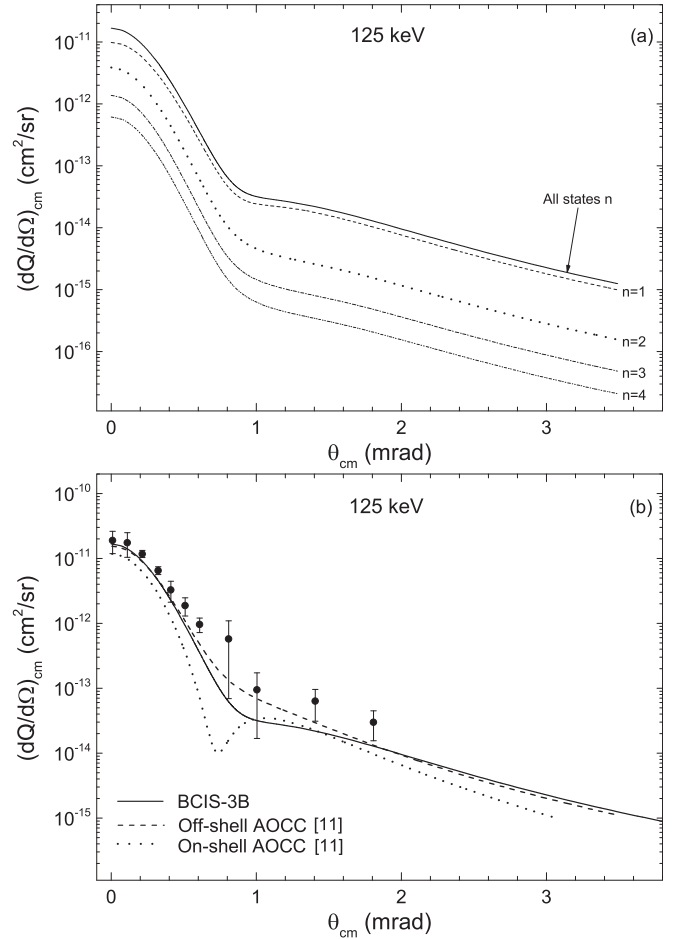


FIG. 6. The same as in Fig. 5, except for the impact energy  $E = 125$  keV and for only one set of the measured cross sections. Experimental data with atomic hydrogen targets: ● Martin *et al.* [100].

[26]. In other words, around  $\theta \approx \theta_{da}$ , the contributions from the repulsive ( $1/R$ ) and attractive ( $-1/s$ ) potentials in the composite interaction  $1/R - 1/s$  are almost equalized. At the given impact energy, the values of  $\theta_{da}$  in the CB1-3B method are slightly shifted for different  $nlm$ . This partially masks the dips in the state-selective cross sections when summing over  $lm$  to obtain  $(dQ/d\Omega)_n^{(\text{CB1-3B})}$ . Further fillings of the dips from each individual state take place after performing the summation over  $n$  to compute  $(dQ/d\Omega)_\Sigma^{(\text{CB1-3B})}$ . As a result, the infinitely low-lying dips are partially filled in the cross sections summed over  $n$  using  $n = 1$  and 2 [26]. Still, the unphysical minimum is not smoothed out even by enlarging the said sum  $\sum_{n=1}^2 (dQ/d\Omega)_n^{(\text{CB1-3B})}$  with the addendum  $\sum_{n=3}^9 (dQ/d\Omega)_n^{(\text{CB1-3B})}$  nor in  $(dQ/d\Omega)_\Sigma^{(\text{CB1-3B})}$  with all the final bound states  $n > 1$  [26].

This is opposite to both the BCIS-3B and the off-shell AOCC methods where, as stated, no minima appear. In the BCIS-3B method, near cancellations of the two potentials in the initial perturbation interaction ( $1/R - 1/s$ ) are entirely masked by the constructive interference terms of highly oscillatory behavior of the electronic full Coulomb wave function (for the on-shell continuum intermediate state) in the

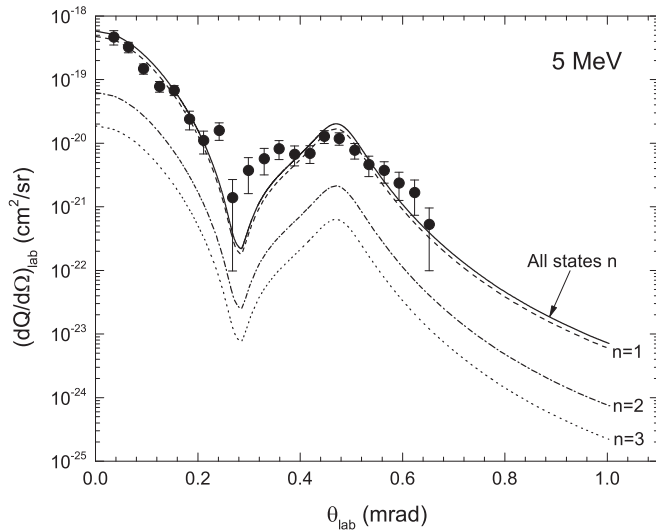


FIG. 7. Differential cross sections  $(dQ/d\Omega)_n$  and  $(dQ/d\Omega)_\Sigma$  (in  $\text{cm}^2/\text{sr}$ ) as a function of scattering angle  $\theta$  (in mrad) at the impact energy  $E = 5$  MeV for electron capture by protons from  $\text{H}(1s)$  into the state-selective states of  $\text{H}(n)$  and into all the states of  $\text{H}(\Sigma)$ . Both the cross sections and the scattering angles are in the laboratory system. Theory: only the present results from the BCIS-3B method. The dashed, dotted-dashed, and dotted curves are for the state-selective cross sections  $(dQ/d\Omega)_1$ ,  $(dQ/d\Omega)_2$ , and  $(dQ/d\Omega)_3$ , respectively, whereas the solid curve is for the state-summed cross section  $(dQ/d\Omega)_\Sigma$  using Eq. (79). Experimental data with atomic hydrogen targets: • Vogt *et al.* [102].

integrand of the transition amplitude. In the off-shell AOCC method, the interaction  $1/R - 1/s$  is not annulled either due the presence of the important effects from the included virtual transitions. The infinitely low-lying dips at varying  $\theta_{\text{da}}$ , typical of the CB1-3B method, are absent from the on-shell AOCC method. Instead of these experimentally undetected dips, the on-shell AOCC predicts one minimum per impact energy located at 1.1, 0.9, and 0.7 mrad for 25, 60, and 125 keV, respectively [11]. The two such situations are also seen in the dotted curves on Fig. 5(b) (0.9 mrad,  $E = 60$  keV) and Fig. 6(b) (0.7 mrad,  $E = 125$  keV).

High-energy theoretical (present) and measured [102] angular distributions are compared in Fig. 7 at  $E_{\text{lab}} = 5$  MeV and a remarkably good agreement is observed. The BCIS-3B method contains the usual second-order effect through double scattering of the captured electron on the two nuclei. This is a quantum-mechanical counterpart of the Thomas classical two-step, billiard-type  $\text{P} - e - \text{T}$  collisions. As stated, in the classical picture, the electron collides first on the projectile nucleus and then on the target nucleus to finally become bound to the projectile. Kinematics of the Thomas double classical scattering is determined by the conservation laws of energy and momenta. As a net result, the projectile itself is deflected through the critical Thomas angle for double scattering (ds),  $\theta_{\text{ds}} = (1/M_p)\sqrt{3}/2$ , in the laboratory system. This critical angle does not depend on either the projectile velocity nor the target mass. In the case of a proton impact,  $\theta_{\text{ds}}$  is located at  $\simeq 0.47$  mrad (lab). The same angle  $\theta_{\text{ds}}$  is also predicted by the second-order quantum-mechanical theories, such as the

BCIS-3B and CDW-3B methods. For proton-hydrogen charge exchange, this prediction has been experimentally confirmed most clearly at 5 MeV [102]. The agreement seen in Fig. 7 at 5 MeV between the BCIS-3B method and the experimental data [102] is especially favorable around the forward and the Thomas peaks. All the state-to-state differential cross sections in the BCIS-3B method also yield the Thomas peaks at the same critical angle  $\theta_{\text{ds}}$ . This is shown in Fig. 7 through the three components  $\{(dQ/d\Omega)_n\}_{n=1,2,3}$  of  $(dQ/d\Omega)_\Sigma$ . Similarly to the two discussed intermediate energies (60 and 125 keV), here too, at 5 MeV, it is noted that  $(dQ/d\Omega)_1$  provides the dominant contribution to  $(dQ/d\Omega)_\Sigma$ . Again, just like the pattern already discussed with Figs. 5 and 6, all the curves for  $\{(dQ/d\Omega)_n\}_{n=1,2,3}$  and  $(dQ/d\Omega)_\Sigma$  possess very similar shapes.

Note that between the forward and the Thomas peak, both the experimental data [102] and the BCIS-3B method exhibit a minimum in the angular distribution at 5 MeV (Fig. 7). However, from the theoretical standpoint, this minimum is of an entirely different nature from the minima near the dark angles appearing at intermediate energies 60 keV (Fig. 5) and 125 keV (Fig. 6), respectively. The experimentally detected minimum is reproduced in second-order theories by the mechanism of a destructive interference from the first- and second-order collisional events. The first-order effects produce the forward peak ( $\theta \approx 0$ ), through a single scattering of the projectile nucleus with the target electron. The second-order effects, via a double scattering of the same target electron on two nuclei, give the Thomas peak at the critical angle,  $\theta_{\text{ds}}$ . It is seen in Fig. 7 that the presently predicted position of the dip is slightly shifted relative to the corresponding angle from the measurement [102]. In the BCIS-3B method, this is not due to adding the contributions from all the final excited states  $\{n, l, m\}$  as evident in Fig. 7 by inspecting the components  $\{(dQ/d\Omega)_n\}_{n=1,2,3}$  of  $(dQ/d\Omega)_\Sigma$ . The cross sections  $(dQ/d\Omega)_\Sigma$ , computed in the BCIS-3B method using (79), have fully converged as a function of increasing  $n$  for all the scattering angles  $\theta$ , including those near and farther away from the minimum. The minimum between the forward and the Thomas peak can only partially be filled by convolving the theoretical cross section  $(dQ/d\Omega)_\Sigma$  with the experimentally estimated folding function [102], as done earlier in Ref. [2] with different second-order methods, e.g., the CDW-3B [18], CB2-3B (the boundary-corrected second Born) [103], and RIA (the reformulated impulse approximation) [104]. Such a convolution has not been made in this work.

The CDW-3B method predicts an experimentally unobserved splitting of the Thomas peak [2]. This splitting into the two adjacent Thomas peaks occurs near the critical angle,  $\theta_{\text{ds}}$ . The reason for this drawback is in the destructive interference effects between the two electronic Coulomb waves from the intermediate ionization channel (one wave in the entrance and the other in the exit channel) [105]. Such an unphysical splitting of the customary Thomas peak can be completely avoided by switching off one of the two electronic Coulomb wave functions while, of course, fully preserving the correct initial and final boundary conditions, as done in the BCIS-3B method. Generally, for angular distributions and their integrated counterparts, the interference effects can both decrease and increase the cross sections depending on

TABLE II. State-selective total cross sections (in  $10^{-16}$  cm<sup>2</sup>) for processes (66), (69), and (75) as a function of impact energy  $E$  (keV/amu) of  $\alpha$  particles for electron capture from H(1s) into the final states ( $n \leq 4$ ) of singly charged positive helium ion He<sup>+</sup>( $nlm$ ). The columns labeled by  $nlm$  refer to the state-selective (or partial) cross sections  $Q_{nlm}$  and  $Q_{nl}$  for (66) and (69), respectively. The rows denoted by  $\Sigma$  represent the cross sections  $Q_{\Sigma}$ , summed over all the final bound states of the He<sup>+</sup>( $nlm$ ) ion, by using Eq. (77). Notation  $X[Z]$  implies  $X \times 10^Z$ .

$nlm \setminus E$ (keV/amu)	10	20	30	50	80	100
100	1.52[+1]	5.34	2.60	9.40[-1]	3.23[-1]	1.83[-1]
200	1.55	1.17	7.52[-1]	3.38[-1]	1.25[-1]	7.06[-2]
210	5.80	4.91	2.99	1.08	2.86[-1]	1.34[-1]
211	1.41	1.08	5.99[-1]	1.86[-1]	4.24[-2]	1.85[-2]
2p	8.62	7.08	4.19	1.45	3.71[-1]	1.71[-1]
300	7.94[-2]	2.20[-1]	2.02[-1]	1.12[-1]	4.50[-2]	2.57[-2]
310	1.63[-1]	6.39[-1]	6.61[-1]	3.53[-1]	1.12[-1]	5.44[-2]
311	2.39[-2]	1.06[-1]	1.06[-1]	5.07[-2]	1.42[-2]	6.55[-3]
3p	2.11[-1]	8.52[-1]	8.73[-1]	4.55[-1]	1.40[-1]	6.75[-2]
320	6.27[-2]	2.90[-1]	2.87[-1]	1.26[-1]	3.03[-2]	1.27[-2]
321	2.34[-2]	1.18[-1]	1.11[-1]	4.40[-2]	9.42[-3]	3.73[-3]
322	3.04[-3]	1.52[-2]	1.36[-2]	5.00[-3]	9.99[-4]	3.83[-4]
3d	1.16[-1]	5.56[-1]	5.36[-1]	2.24[-1]	5.11[-2]	2.09[-2]
400	1.43[-2]	7.00[-2]	7.77[-2]	4.85[-2]	2.02[-2]	1.16[-2]
410	2.58[-2]	1.75[-1]	2.30[-1]	1.48[-1]	5.09[-2]	2.53[-2]
411	3.04[-3]	2.62[-2]	3.42[-2]	2.00[-2]	6.17[-3]	2.91[-3]
4p	3.19[-2]	2.27[-1]	2.98[-1]	1.88[-1]	6.33[-2]	3.11[-2]
420	1.03[-2]	8.59[-2]	1.15[-1]	6.52[-2]	1.77[-2]	7.62[-3]
421	3.09[-3]	3.18[-2]	4.20[-2]	2.17[-2]	5.26[-3]	2.15[-3]
422	3.39[-4]	3.85[-3]	4.85[-3]	2.33[-3]	5.32[-4]	2.12[-4]
4d	1.71[-2]	1.57[-1]	2.09[-1]	1.13[-1]	2.93[-2]	1.24[-2]
430	1.22[-3]	1.26[-2]	1.66[-2]	7.94[-3]	1.67[-3]	6.26[-4]
431	5.86[-4]	6.95[-3]	9.01[-3]	4.03[-3]	7.83[-4]	2.82[-4]
432	1.35[-4]	1.76[-3]	2.17[-3]	8.98[-4]	1.62[-4]	5.61[-5]
433	1.33[-5]	1.73[-4]	2.04[-4]	8.06[-5]	1.40[-5]	4.76[-6]
4f	2.69[-3]	3.03[-2]	3.93[-2]	1.80[-2]	3.59[-3]	1.31[-3]
$\Sigma$	2.60[+1]	1.65[+1]	1.08[+1]	4.46	1.35	6.83[-1]
$nlm \setminus E$ (keV/amu)	150	200	300	500	800	1000
100	5.84[-2]	2.35[-2]	5.57[-3]	7.08[-4]	8.51[-5]	2.92[-5]
200	2.08[-2]	7.60[-3]	1.53[-3]	1.57[-4]	1.59[-5]	5.10[-6]
210	2.73[-2]	7.61[-3]	1.04[-3]	6.48[-5]	4.13[-6]	1.06[-6]
211	3.37[-3]	8.77[-4]	1.11[-4]	6.55[-6]	4.10[-7]	1.05[-7]
2p	3.41[-2]	9.37[-3]	1.26[-3]	7.79[-5]	4.95[-6]	1.27[-6]
300	7.58[-3]	2.73[-3]	5.31[-4]	5.22[-5]	5.10[-6]	1.61[-6]
310	1.14[-2]	3.16[-3]	4.20[-4]	2.52[-5]	1.56[-6]	3.95[-7]
311	1.26[-3]	3.30[-4]	4.17[-5]	2.42[-6]	1.49[-7]	3.82[-8]
3p	1.39[-2]	3.82[-3]	5.04[-4]	3.01[-5]	1.86[-6]	4.71[-7]
320	1.97[-3]	4.33[-4]	4.11[-5]	1.58[-6]	6.36[-8]	1.31[-8]
321	5.27[-4]	1.10[-4]	9.76[-6]	3.55[-7]	1.38[-8]	2.82[-9]
322	5.13[-5]	1.03[-5]	8.83[-7]	3.12[-8]	1.22[-9]	2.51[-10]
3d	3.12[-3]	6.73[-4]	6.24[-5]	2.35[-6]	9.37[-8]	1.92[-8]
400	3.44[-3]	1.23[-3]	2.37[-4]	2.29[-5]	2.21[-6]	6.97[-7]
410	5.38[-3]	1.49[-3]	1.97[-4]	1.17[-5]	7.11[-7]	1.79[-7]
411	5.70[-4]	1.51[-4]	1.90[-5]	1.10[-6]	6.73[-8]	1.72[-8]
4p	6.52[-3]	1.79[-3]	2.35[-4]	1.38[-5]	8.46[-7]	2.14[-7]
420	1.22[-3]	2.70[-4]	2.56[-5]	9.75[-7]	3.89[-8]	7.99[-9]
421	3.15[-4]	6.63[-5]	5.94[-6]	2.15[-7]	8.38[-9]	1.71[-9]
422	2.97[-5]	6.07[-6]	5.26[-7]	1.87[-8]	7.31[-10]	1.51[-10]
4d	1.91[-3]	4.14[-4]	3.85[-5]	1.44[-6]	5.72[-8]	1.17[-8]
430	7.51[-5]	1.33[-5]	9.09[-7]	2.22[-8]	5.79[-10]	9.65[-11]
431	3.15[-5]	5.38[-6]	3.50[-7]	8.22[-9]	2.09[-10]	3.46[-11]
432	5.89[-6]	9.63[-7]	5.93[-8]	1.32[-9]	3.26[-11]	5.35[-12]
433	4.85[-7]	7.76[-8]	4.66[-9]	1.02[-10]	2.55[-12]	4.23[-13]
4f	1.51[-4]	2.62[-5]	1.74[-6]	4.15[-8]	1.07[-9]	1.77[-10]
$\Sigma$	1.69[-1]	5.65[-2]	1.08[-2]	1.13[-3]	1.21[-4]	4.00[-5]

the considered impact energies. For example, in the CDW-3B method, below 100 keV/amu, the values of  $Q^{(\text{CDW-3B})}$  are systematically increased by the constructive interference effects from the two electronic Coulomb waves. As a result, therein, there is a large departure of the CDW-3B method from the associated experimental data. This failure too is foreign to the BCIS-3B method on account of dealing with only one electronic Coulomb wave. Moreover, as opposed to the CDW-3B method, the initial total scattering state in the prior BCIS-3B method is normalized at all interparticle distances. Further,  $Q^{(\text{BCIS-3B})}$  is usually peaked near the Massey maximum, while  $Q^{(\text{CDW-3B})}$  keeps on rising with decreased impact energy, at variance with measurements. The Massey peak occurs when the projectile velocity  $v$  matches the average velocity  $v_e$  of the electron on the shell from which capture takes place. As per, e.g., Fig. 1(a), this occurs around 25 keV for the resonant electron-transfer process  $\text{H}^+ + \text{H}(1s) \rightarrow \text{H}(1s) + \text{H}^+$ .

#### D. Electron capture from H(1s) by $\alpha$ particles into any excited states of the helium ion $\text{He}^+(nlm)$

Next, we pass to processes (66), (69), (72), and (75). Table II reports on the state-selective total cross sections in the BCIS-3B method for  $\alpha$ -H charge exchange at impact energies  $10 \text{ keV/amu} \leq E \leq 1000 \text{ keV/amu}$ . Using some of these results, Fig. 8 deals particularly with  $Q_{2s}$  and  $Q_{2p}$  in relation to process (69) for  $n = 2$  with  $l = 0$  and 1, respectively. The literature has no reported data on  $Q_{2p}$ . On the other hand, measured data on  $Q_{2s}$  are available [106] and are seen in

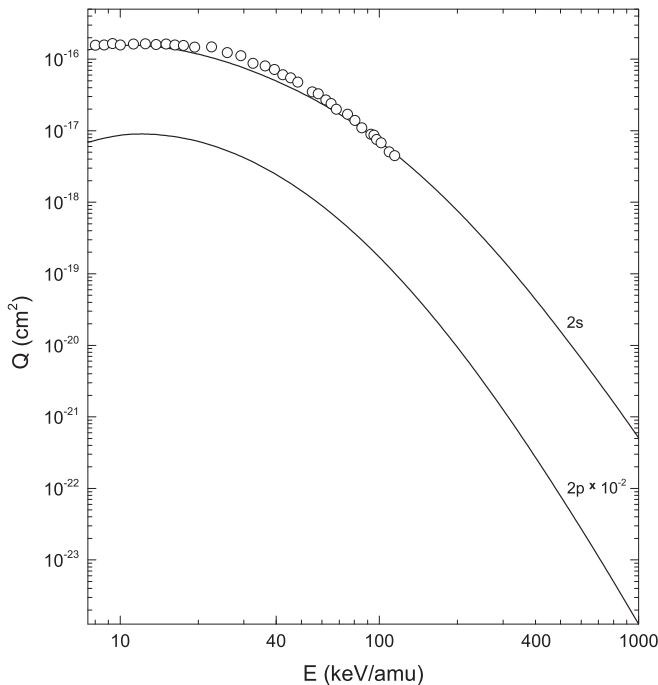


FIG. 8. State-selective total cross sections  $Q_{2s}$  and  $Q_{2p}$  in  $\text{cm}^2$  as a function of impact energies  $E$  (keV/amu) for electron capture by alpha particles from H(1s), as per process (69). The curves are the present results from the BCIS-3B method. Experimental data with atomic hydrogen targets:  $\circ$  ( $Q_{2s}$ ) Shah and Gilbody [106]. The theoretical results for  $Q_{2p}$  are divided by  $10^2$ .

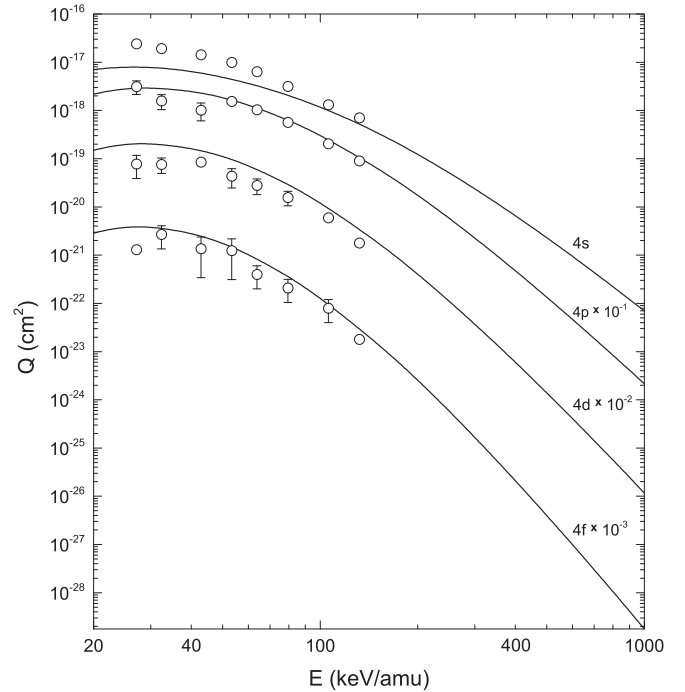


FIG. 9. State-selective total cross sections  $Q_{4s}$ ,  $Q_{4p}$ ,  $Q_{4d}$ , and  $Q_{4f}$  in  $\text{cm}^2$  as a function of impact energies  $E$  (keV/amu) for electron capture by alpha particles from H(1s), as per process (69). The curves are the present results from the BCIS-3B method. Experimental data with atomic hydrogen targets:  $\circ$  ( $Q_{4s}$ ,  $Q_{4p}$ ,  $Q_{4d}$ ,  $Q_{4f}$ ) Frieling *et al.* [107]. Both the theoretical and experimental results are divided by a factor:  $Q_{4p}$  by  $10$ ,  $Q_{4d}$  by  $10^2$ , and  $Q_{4f}$  by  $10^3$ .

Fig. 8 to be in excellent agreement with the BCIS-3B method. This accord persists throughout the overlapped region even at energies as low as  $E = 8 \text{ keV/amu}$ , which is unprecedented within the category of high-energy theories to which the BCIS-3B method belongs.

Formations of some of the higher excited states via  $\text{He}^+(nl)$  and  $\text{He}^+(n)$  for  $n = 4$  in processes (69) with  $l = 0, 1, 2, 3$  and (72) are considered in Figs. 9 and 10, respectively. Qualitatively, Fig. 9 shows a concordant behavior of the line shapes of the theoretical and experimental data for  $Q_{4p}$ ,  $Q_{4d}$ , and  $Q_{4f}$ . Quantitatively, the BCIS-3B method and measurement are in very good agreement for  $Q_{4p}$  and  $Q_{4f}$ . As to  $Q_{4s}$  and  $Q_{4d}$ , the theory underestimates and overestimates, respectively, the corresponding experimental data. However, when the theoretical cross sections  $Q_{4s}$ ,  $Q_{4p}$ ,  $Q_{4d}$ , and  $Q_{4f}$  are summed up, the predictions of  $Q_n$  for  $n = 4$  in the BCIS-3B method are found in Fig. 10 to excellently reproduce the measured data [107] for  $Q_4$  at all energies.

The symbols (open circles) plotted in Figs. 9 and 10 refer to the same experiment from Ref. [107]. In fact, in Ref. [107] only the cross sections  $Q_n$  for  $n = 4$  summed over all the subshells  $0 \leq l \leq 3$  have been measured. On the other hand, none of the individual cross sections  $Q_{4s}$ ,  $Q_{4p}$ ,  $Q_{4d}$ , nor  $Q_{4f}$  has been measured in Ref. [107]. Instead, they were computationally estimated in Ref. [107] from the measured data for  $Q_4$  by an extrapolation procedure, which might be prone to inaccuracies. This limitation should be kept in mind when revisiting Fig. 9, where the data from Ref. [107] on

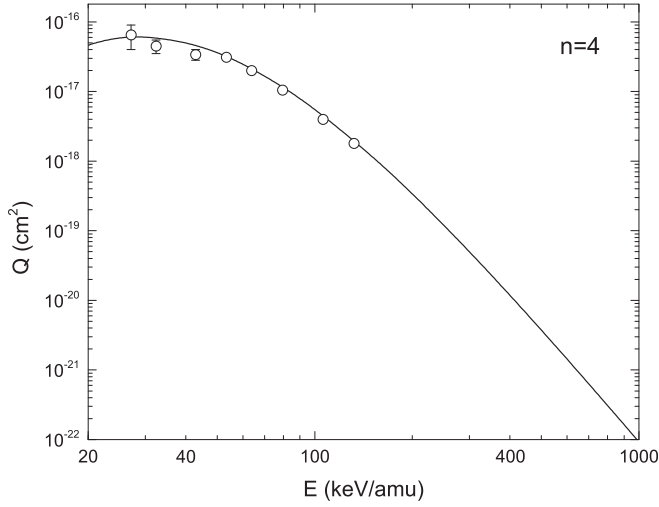


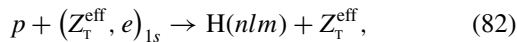
FIG. 10. State-selective total cross sections  $Q_4$  ( $\text{cm}^2$ ) as a function of impact energies  $E$  (keV/amu) for electron capture by alpha particles from  $\text{H}(1s)$ , as per process (72). The curve is the present result from the BCIS-3B method. Experimental data with atomic hydrogen targets:  $\circ$  Frieling *et al.* [107].

$Q_{4s}$ ,  $Q_{4p}$ ,  $Q_{4d}$ , and  $Q_{4f}$  (open circles) are compared with the theoretical findings. Note that in Figs. 9 and 10 both the experiment [107] and the BCIS-3B method refer to hydrogen atoms as the targets.

For process (75), the theoretical total cross sections  $Q_\Sigma$ , summed over all the excited states using the Oppenheimer  $n^{-3}$  scaling rule (77), are shown in Fig. 11 together with the measured findings [94,106,108–114]. Some of the displayed experimental data are on  $\text{H}_2$  as the target and these are converted to atomic hydrogen targets by the prescription of Ref. [89]. Nearly all the experimental data available in the literature are plotted in this figure. It is evident that the experimental data on  $Q_\Sigma$  for hydrogen targets impacted by alpha particles (Fig. 11) versus those by protons (Fig. 4) are more dispersed for the former than for the latter projectiles. For example, significant deviations from the joint trend of the other measured  $Q_\Sigma$  are seen on Fig. 11 below 40 keV/amu and above 250 keV/amu in the experimental data from Refs. [111] and [112], respectively. Nevertheless, most experimental data seen in Fig. 11 are mutually concordant. Moreover, they are in excellent agreement with  $Q_\Sigma$  from the BCIS-3B method. This observation coheres with the like conclusion on the  $p$ -hydrogen collisions for both total and differential cross sections.

### E. Electron capture from $\text{He}(1s^2)$ by protons into any excited states of hydrogen $\text{H}(nlm)$

In this section, we proceed with tackling processes (67), (70), (73), and (76). These are approximated by their effective hydrogenlike substitutes generated from the prototype:



which coincides with (7) when  $Z_T$  is replaced by  $Z_T^{\text{eff}}$ . As mentioned, in the effective charge  $Z_T^{\text{eff}}$ , the target nuclear charge  $Z_T$  is shielded by the Slater screening  $Z_s = \frac{5}{16}$  giving

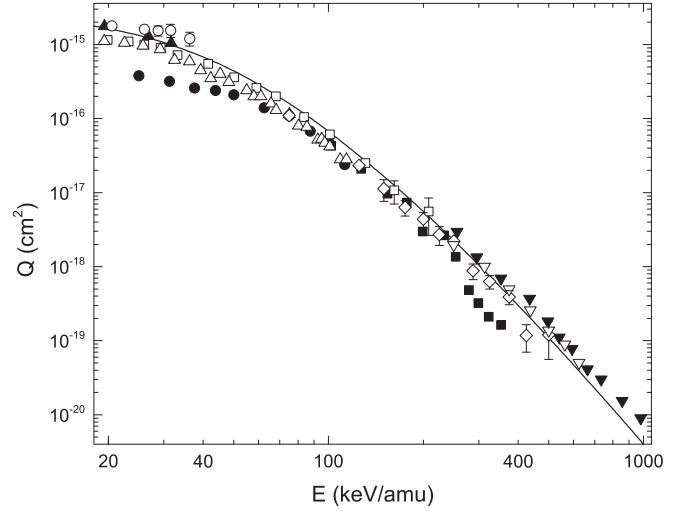


FIG. 11. State-summed total cross sections in  $Q_\Sigma$  ( $\text{cm}^2$ ) as a function of impact energies  $E$  (keV/amu) for electron capture into all the final bound states  $\text{He}^+(\Sigma)$  from the ground state of hydrogen by alpha particles, as per process (75):  $\alpha + \text{H}(1s) \rightarrow \text{He}^+(\Sigma) + p$ . The curve is the present result from the BCIS-3B method for  $Q_\Sigma \simeq Q_1 + Q_2 + Q_3 + 2.561Q_4$  from (77). Experimental data with atomic hydrogen targets:  $\circ$  Bayfield and Khayrallah [108],  $\square$  Olson *et al.* [109],  $\triangle$  Shah and Gilbody [106],  $\diamond$  Hvelplund and Andersen [94],  $\nabla$  Sant'Anna *et al.* [110]. Experimental data with molecular hydrogen targets (converted to atomic hydrogen targets following Ref. [89]):  $\bullet$  Allison [111],  $\blacksquare$  Pivovar *et al.* [112],  $\blacktriangle$  Bayfield and Khayrallah [113],  $\blacktriangledown$  Hvelplund *et al.* [114].

$Z_T^{\text{eff}} = Z_T - Z_s = 1.6875$ . This is one of the two remainders of the original four-body problem in the  $p$ -He collisions with single charge exchange. The other remainder is a factor of 2 by which the effective three-body cross sections for (82) should be multiplied to account for an equal chance of capturing either  $e_1$  or  $e_2$  via the original process (63), whose examples are (67), (70), (73), and (76).

Experimental data are available for  $Q_{2s}$ ,  $Q_{2p}$ ,  $Q_{3s}$ ,  $Q_{3p}$ ,  $Q_{3d}$ ,  $Q_{4s}$ , and  $Q_\Sigma$  [84,86,88,97,115–126]. Generally, the existing measured cross sections are mutually in very good accord for  $Q_{2s}$ ,  $Q_{3s}$ ,  $Q_{3p}$ ,  $Q_{4s}$ , and  $Q_\Sigma$ . Thus far, no measurement has been reported on  $Q_{4p}$ ,  $Q_{4d}$ , and  $Q_{4f}$  for process (70) with  $n = 4$ .

The theoretical state-selective total cross sections within the energy range  $10 \text{ keV} \leq E \leq 1000 \text{ keV}$  are stored in Table III. In order to illustrate these cross sections graphically, Figs. 12–15 are presented for processes (70) and (76) at energies overlapping those from the experimental data. Regarding the process (70), we allocate Fig. 12 for  $Q_{2s}$ ,  $Q_{2p}$ , Fig. 13 for  $Q_{3s}$ ,  $Q_{3p}$ ,  $Q_{3d}$ , and Fig. 14 for  $Q_{4s}$ ,  $Q_{4p}$ ,  $Q_{4d}$ ,  $Q_{4f}$ . Figure 15 is for process (76).

Since we are dealing with the inherently four-body processes (67), (70), (73), and (76), that we presently treat as the effective three-body collisions, some discrepancies are expected between the BCIS-3B method and experiments. However, as one can see from Figs. 12–14, at all the considered impact energies, the present theoretical predictions are in excellent agreement with the experimentally determined cross sections for spherically symmetrical final hydrogenlike

TABLE III. State-selective total cross sections (in  $10^{-16}$  cm $^2$ ) for processes (67), (70), and (76) as a function of impact energy  $E$  (keV) of protons for single-electron capture from He( $1s^2$ ) into all final states of atomic hydrogen with  $n \leq 4$ . The columns labeled by  $nlm$  refer to the state-selective (or partial) cross sections  $Q_{nlm}$  and  $Q_{nl}$  for (67) and (70), respectively. The rows denoted by  $\Sigma$  represent the cross sections  $Q_{\Sigma}$ , summed over all the final bound states of the H( $nlm$ ) atom, by using Eq. (77). Notation  $X[Z]$  implies  $X \times 10^Z$ .

$nlm \setminus E$ (keV)	10	20	30	50	80	100
100	1.28[-1]	5.49[-1]	8.24[-1]	7.15[-1]	3.64[-1]	2.26[-1]
200	4.62[-3]	1.74[-2]	3.90[-2]	5.85[-2]	4.16[-2]	2.86[-2]
210	1.13[-3]	3.88[-3]	6.06[-3]	8.94[-3]	6.71[-3]	4.59[-3]
211	4.50[-5]	3.18[-4]	9.68[-4]	1.57[-3]	1.05[-3]	6.76[-4]
2p	1.22[-3]	4.52[-3]	8.00[-3]	1.21[-2]	8.81[-3]	5.94[-3]
300	1.14[-3]	4.12[-3]	9.44[-3]	1.57[-2]	1.20[-2]	8.40[-3]
310	3.26[-4]	1.18[-3]	1.76[-3]	2.72[-3]	2.21[-3]	1.56[-3]
311	1.31[-5]	7.85[-5]	2.57[-4]	4.70[-4]	3.41[-4]	2.26[-4]
3p	3.52[-4]	1.34[-3]	2.27[-3]	3.66[-3]	2.89[-3]	2.01[-3]
320	8.88[-6]	4.82[-5]	6.55[-5]	7.81[-5]	5.90[-5]	4.04[-5]
321	1.22[-6]	4.40[-6]	1.18[-5]	2.62[-5]	2.09[-5]	1.38[-5]
322	3.72[-8]	4.16[-7]	1.67[-6]	3.35[-6]	2.40[-6]	1.53[-6]
3d	1.14[-5]	5.78[-5]	9.24[-5]	1.37[-4]	1.06[-4]	7.10[-5]
400	4.52[-4]	1.61[-3]	3.71[-3]	6.37[-3]	4.99[-3]	3.53[-3]
410	1.33[-4]	5.01[-4]	7.34[-4]	1.15[-3]	9.60[-4]	6.83[-4]
411	5.47[-6]	3.10[-5]	1.04[-4]	1.98[-4]	1.48[-4]	9.87[-5]
4p	1.44[-4]	5.63[-4]	9.41[-4]	1.54[-3]	1.25[-3]	8.81[-4]
420	4.86[-6]	2.74[-5]	3.73[-5]	4.43[-5]	3.43[-5]	2.37[-5]
421	6.75[-7]	2.42[-6]	6.29[-6]	1.46[-5]	1.20[-5]	8.06[-6]
422	2.06[-8]	2.15[-7]	8.86[-7]	1.86[-6]	1.38[-6]	8.87[-7]
4d	6.25[-6]	3.27[-5]	5.17[-5]	7.72[-5]	6.11[-5]	4.16[-5]
430	3.78[-8]	3.16[-7]	4.97[-7]	5.54[-7]	3.82[-7]	2.50[-7]
431	1.04[-8]	4.90[-8]	9.02[-8]	2.07[-7]	1.82[-7]	1.21[-7]
432	8.37[-10]	4.42[-9]	1.95[-8]	5.32[-8]	4.31[-8]	2.76[-8]
433	2.39[-11]	4.64[-10]	2.30[-9]	5.41[-9]	4.03[-9]	2.51[-9]
4f	6.03[-8]	4.24[-7]	7.21[-7]	1.08[-6]	8.40[-7]	5.53[-7]
$\Sigma$	1.37[-1]	5.82[-1]	8.95[-1]	8.25[-1]	4.45[-1]	2.82[-1]
$nlm \setminus E$ (keV)	150	200	300	500	800	1000
100	7.58[-2]	2.98[-2]	6.56[-3]	7.39[-4]	7.97[-5]	2.62[-5]
200	1.07[-2]	4.34[-3]	9.62[-4]	1.06[-4]	1.10[-5]	3.56[-6]
210	1.60[-3]	5.93[-4]	1.09[-4]	8.70[-6]	6.41[-7]	1.73[-7]
211	2.13[-4]	7.37[-5]	1.24[-5]	9.08[-7]	6.29[-8]	1.66[-8]
2p	2.03[-3]	7.40[-4]	1.34[-4]	1.05[-5]	7.67[-7]	2.06[-7]
300	3.22[-3]	1.32[-3]	2.93[-4]	3.20[-5]	3.32[-6]	1.07[-6]
310	5.63[-4]	2.11[-4]	3.90[-5]	3.12[-6]	2.29[-7]	6.15[-8]
311	7.36[-5]	2.58[-5]	4.39[-6]	3.22[-7]	2.23[-8]	5.88[-9]
3p	7.10[-4]	2.63[-4]	4.77[-5]	3.76[-6]	2.73[-7]	7.33[-8]
320	1.34[-5]	4.53[-6]	6.91[-7]	4.03[-8]	2.09[-9]	4.70[-10]
321	4.19[-6]	1.33[-6]	1.87[-7]	9.94[-9]	4.83[-10]	1.06[-10]
322	4.36[-7]	1.33[-7]	1.77[-8]	8.87[-10]	4.12[-11]	8.92[-12]
3d	2.26[-5]	7.46[-6]	1.10[-6]	6.20[-8]	3.14[-9]	7.00[-10]
400	1.37[-3]	5.62[-4]	1.25[-4]	1.36[-5]	1.41[-6]	4.55[-7]
410	2.50[-4]	9.42[-5]	1.75[-5]	1.40[-6]	1.02[-7]	2.75[-8]
411	3.26[-5]	1.15[-5]	1.96[-6]	1.44[-7]	9.94[-9]	2.62[-9]
4p	3.16[-4]	1.17[-4]	2.14[-5]	1.68[-6]	1.22[-7]	3.28[-8]
420	7.96[-6]	2.72[-6]	4.16[-7]	2.43[-8]	1.26[-9]	2.83[-10]
421	2.49[-6]	7.95[-7]	1.12[-7]	5.98[-9]	2.91[-10]	6.39[-11]
422	2.57[-7]	7.92[-8]	1.06[-8]	5.32[-10]	2.48[-11]	5.36[-12]
4d	1.34[-5]	4.47[-6]	6.61[-7]	3.73[-8]	1.89[-9]	4.22[-10]
430	7.42[-8]	2.25[-8]	2.79[-9]	1.17[-10]	4.21[-12]	7.87[-13]
431	3.50[-8]	1.02[-8]	1.19[-9]	4.67[-11]	1.61[-12]	2.96[-13]
432	7.39[-9]	2.05[-9]	2.24[-10]	8.11[-12]	2.63[-13]	4.73[-14]
433	6.44[-10]	1.74[-10]	1.83[-11]	6.36[-13]	2.00[-14]	3.54[-15]
4f	1.60[-7]	4.73[-8]	5.66[-9]	2.27[-10]	8.00[-12]	1.48[-12]
$\Sigma$	9.68[-2]	3.82[-2]	8.38[-3]	9.30[-4]	9.90[-5]	3.23[-5]

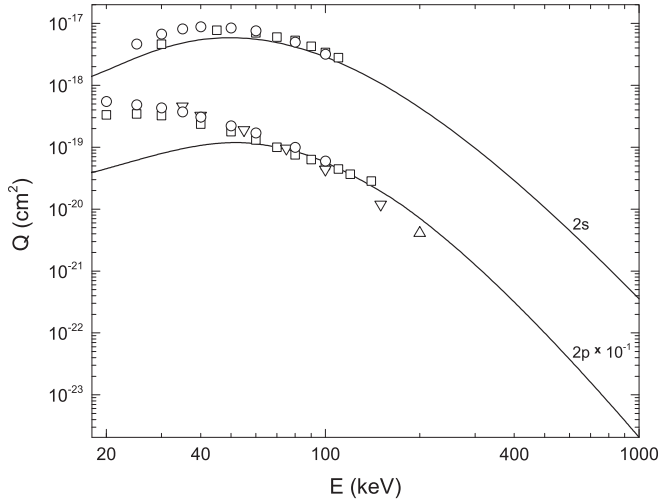


FIG. 12. State-selective total cross sections  $Q_{2s}$  and  $Q_{2p}$  in  $\text{cm}^2$  as a function of impact energy  $E$  (keV) for single-electron capture by protons from  $\text{He}(1s^2)$ , as per process (70). The curves are the present results from the BCIS-3B method with the effective hydrogenic model (see the main text). Experimental data:  $\square$  ( $Q_{2s}$ ,  $Q_{2p}$ ) Hughes *et al.* [84],  $\circ$  ( $Q_{2s}$ ,  $Q_{2p}$ ) Cline *et al.* [115],  $\triangle$  ( $Q_{2p}$ ) Hippler *et al.* [116],  $\nabla$  ( $Q_{2p}$ ) Hippler *et al.* [117]. Both the theoretical and experimental results for  $Q_{2p}$  are divided by 10.

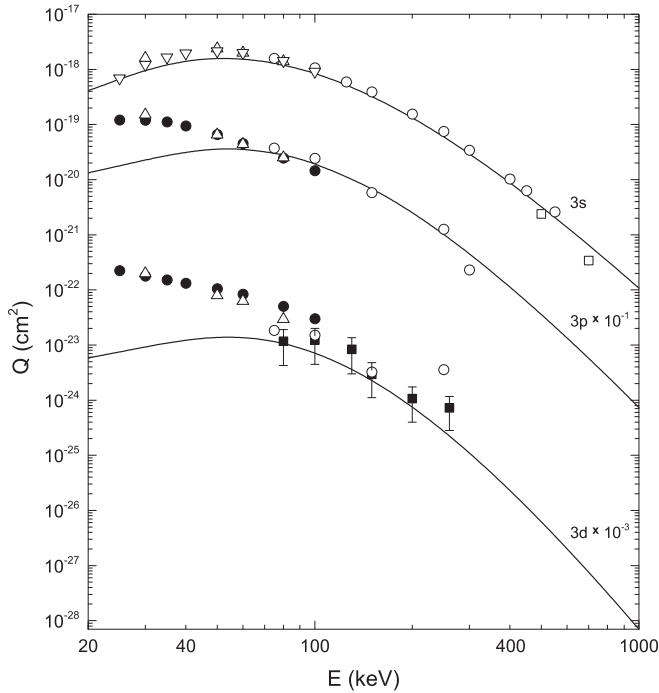


FIG. 13. State-selective total cross sections  $Q_{3s}$ ,  $Q_{3p}$ , and  $Q_{3d}$  in  $\text{cm}^2$  as a function of impact energy  $E$  (keV) for single-electron capture by protons from  $\text{He}(1s^2)$ , as per process (70). The curves are the present results from the BCIS-3B method with the effective hydrogenic model (see the main text). Experimental data:  $\circ$  ( $Q_{3s}$ ,  $Q_{3p}$ ,  $Q_{3d}$ ) Ford *et al.* [88],  $\square$  ( $Q_{3s}$ ) Conrads and Nichols [118],  $\triangle$  ( $Q_{3s}$ ,  $Q_{3p}$ ,  $Q_{3d}$ ) Brower and Pipkin [119],  $\nabla$  ( $Q_{3s}$ ) Cline *et al.* [115],  $\bullet$  ( $Q_{3p}$ ,  $Q_{3d}$ ) Cline *et al.* [120],  $\blacksquare$  ( $Q_{3d}$ ) Edwards and Thomas [121]. Both the theoretical and experimental results are divided by a factor:  $Q_{3p}$  by 10 and  $Q_{3d}$  by  $10^3$ .

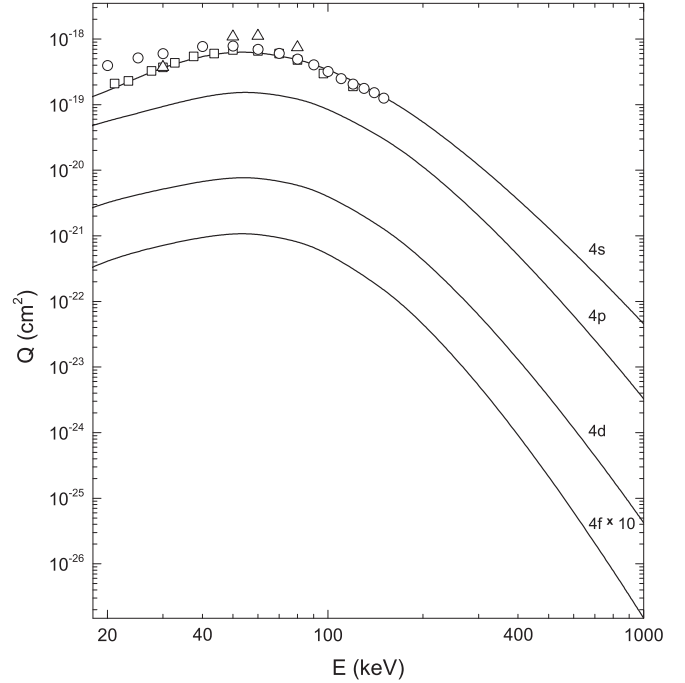


FIG. 14. State-selective total cross sections  $Q_{4s}$ ,  $Q_{4p}$ ,  $Q_{4d}$ , and  $Q_{4f}$  in  $\text{cm}^2$  as a function of impact energy  $E$  (keV) for single-electron capture by protons from  $\text{He}(1s^2)$ , as per process (70). The curves are the present results from the BCIS-3B method with the effective hydrogenic model (see the main text). Experimental data:  $\square$  ( $Q_{4s}$ ) Hughes *et al.* [86],  $\circ$  ( $Q_{4s}$ ) Doughty *et al.* [122],  $\triangle$  ( $Q_{4s}$ ) Brower and Pipkin [119]. The theoretical results for  $Q_{4f}$  are multiplied by 10.

states ( $l = 0$ ), such as  $Q_{2s}$  ( $E \in [25, 115]$  keV),  $Q_{3s}$  ( $E \in [25, 700]$  keV), and  $Q_{4s}$  ( $E \in [20, 150]$  keV). For nonspherical states ( $l \neq 0$ ), the theory and experiments are also in excellent agreement for  $Q_{2p}$  ( $E \in [50, 200]$  keV),  $Q_{3p}$  ( $E \in [50, 300]$  keV), and  $Q_{3d}$  ( $E \in [70, 250]$  keV). On the other hand, it is apparent from Figs. 12 and 13 that the BCIS-3B method significantly underestimates the experimental data below 50 keV ( $Q_{2p}$ ,  $Q_{3p}$ ) and below 70 keV ( $Q_{3d}$ ).

Another way to compute any state-selective cross sections (including  $Q_{3p}$  and  $Q_{3d}$  in order to readdress the said underestimation issue) could be to apply the BCIS-4B method directly to the original four-body problem (63) instead of tackling its substitute (82), which is the three-body effective problem. Such a more flexible approach would permit the use of a better ansatz than the simplest one-parameter uncorrelated ground-state closed-shell ( $1s^2$ ) helium wave function given by Hylleraas [127]. This is what has been done in the CB1-4B method [72] by employing the two-parameter highly radially correlated open-shell ( $1s1s'$ ) ground-state helium wave function of Silverman *et al.* [128]. However, while dealing with, e.g.,  $Q_{3p}$  and  $Q_{3d}$ , the CB1-4B method for the purely four-body problem (63) has also been found [72] to exhibit precisely the same pattern as the mentioned underestimation in the BCIS-3B method for the effective three-body problem (82).

This coheres with the earlier findings in, e.g., the four-body continuum-distorted-wave (CDW-4B) method [129,130]. For instance, in Ref. [129], the 35-parameter configuration-

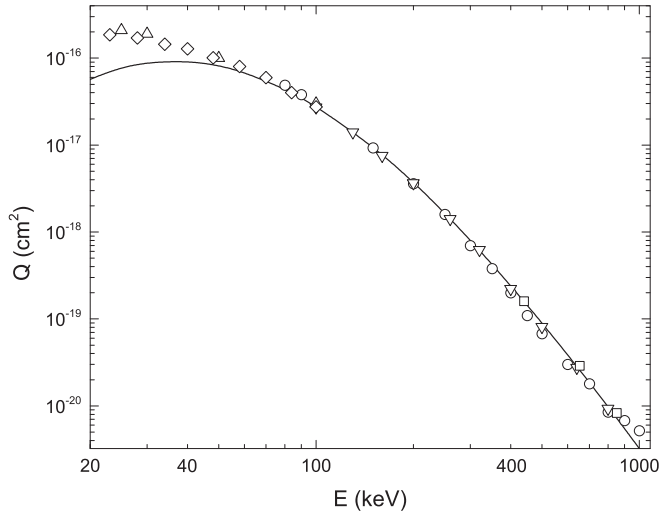


FIG. 15. State-summed total cross sections  $Q_{\Sigma}$  ( $\text{cm}^2$ ) as a function of impact energy  $E$  (keV) for single-electron capture into all the final bound states  $H(\Sigma)$  from the ground state of helium by protons, as per process (76). The curves are the present results from the BCIS-3B method for  $Q_{\Sigma} \simeq Q_1 + Q_2 + Q_3 + 2.561Q_4$  from (77) with the effective hydrogenic model (see the main text). Experimental data:  $\square$  Welsh *et al.* [97],  $\circ$  Williams [123],  $\triangle$  Martin *et al.* [124],  $\nabla$  Shah and Gilbody [125],  $\diamond$  Shah *et al.* [126].

interaction (CI) ground-state helium wave function of Weiss [131] has been used, with 99% of electron correlation energy. Therein, it has been shown that, as opposed to low and high energies, the static interelectron correlations in the ground state of helium play only a minor role at intermediate energies. Hence, a better helium wave function would hardly be able to significantly reduce the extent of underestimation of the measured  $Q_{3p}$  and  $Q_{3d}$  by perturbative theories. Rather, hopefully, some new measurements would have a better chance to help clarify the situation with, for example,  $Q_{3p}$  and  $Q_{3d}$ , especially given that the existing experimental data for, e.g.,  $Q_{3d}$  at 250 keV (open circle) [88] in Fig. 13 are quite far off the trend of the remaining experimental data.

More generally, what is much needed for a more thorough benchmarking of the existing perturbative theories are some additional experiments on  $Q_{nl}$  from about 100 to 500–700 keV. Often, these theories (for both  $p$ -H and  $p$ -He charge exchange) are in significant disagreement especially for non-spherical final states [1]. We are well aware of the fact that at higher energies, measurements on  $Q_{nl}$  for  $l \neq 0$  are very difficult. Customarily, energies of barely a few tens of keV are outside the primary applicability domain of most perturbative theories. Nevertheless, according to our computations, the BCIS-3B method appears to handle quite well (admittedly with some exceptions) even the region of a few tens of keV at least for the collisional systems under study. It remains to be seen, however, whether this appealing feature of the BCIS-3B method would systematically persist also for other scattering aggregates beyond the present investigations.

Finally, in Fig. 15, the experimental data on  $Q_{\Sigma}$  for process (76) are compared with the cross sections from the BCIS-3B method. The pertinent theoretical results on  $Q_{\Sigma}$  for any final bound state, obtained by means of Eq. (77), refer to the

effective hydrogenic model problem:

$$p + (Z_{\tau}^{\text{eff}}, e)_{1s} \rightarrow H(\Sigma) + Z_{\tau}^{\text{eff}}, \quad (83)$$

with  $Z_{\tau}^{\text{eff}} = 1.6875$  in place of the bare helium nuclear charge  $Z_{\tau} = 2$  which appears in the original process (76). The BCIS-3B method is seen in Fig. 15 to be in perfect agreement with the experimental data over a wide range of impact energies,  $40 \leq E \leq 1000$  keV. This extends the applicability domain of the present theory even below its lower-energy limit of anticipated validity.

#### IV. CONCLUSION

Single charge exchange in collisions between fast bare projectiles and hydrogenlike atomic systems is investigated by means of the prior version of the three-body boundary-corrected continuum-intermediate-states (BCIS-3B) method. In this second-order method, from the category of high-energy theories, the transient ionization channel is included through the electronic continuum intermediate states. Such states, in the prior transition amplitude, are described by the full Coulomb wave function centered on the target nuclear charge  $Z_{\tau}$ . Here, the underlying two-step mechanism is mediated by this intermediate channel, which allows the electron to be captured from an on-shell continuum state of the target.

This study is focused on developing a general computer code in the BCIS-3B method for one-electron capture by a heavy projectile nucleus of an arbitrary charge  $Z_p$  from the ground state of a hydrogenlike target  $Z_p + (Z_{\tau}, e)_{1s} \rightarrow (Z_p, e)_{nlm} + Z_{\tau}$ , where  $\{n, l, m\}$  is the usual triple of quantum numbers (principal, angular, magnetic). For this goal, we designed a semianalytical procedure consisting of two stages. First, the results of four successive integrals from the original six-dimensional integration for the transition amplitude are calculated by analytical means yielding the explicit exact closed forms. The remaining two integrals are computed accurately by numerical quadratures over real variables in finite intervals. One of these two integrals is a smooth Feynman parametrization integral which is suitable for robust numerical computations. The other integral comes from the usual integral representation of the Kummer confluent hypergeometric function with two branch-point singularities at 0 and 1 (the two ends of the integration interval). Both singularities are integrable by using the standard Cauchy regularization of the integrand performed simultaneously for the points 0 and 1. This renders the Kummer integral smoother and, as such, amenable to a precise numerical quadrature.

With these semianalytical findings at hand, the cross sections integrated over all the scattering angles (or over the transverse momentum transfer), i.e., total cross sections  $Q_{nlm}$ , are reduced to a three-dimensional numerical quadrature. All the numerical integrations are carried out by using the Gauss-Legendre quadrature rule. For the outermost integration over the transverse momentum transfer in total cross sections, we use the adaptive Gauss-Legendre quadrature where the integration variable is scaled to acknowledge the dominant contribution arising from the vicinity of the forward cone for scattering angles. To monitor the accuracy of the numerical work, the integration order (the number of pivots and weights per each quadrature axis) is systematically augmented until

full convergence to two decimal places has been achieved in all the presently reported computations.

The ensuing computer code for the BCIS-3B method, based upon the expounded semianalytical procedures, refers to the  $1s \rightarrow nlm$  transitions in collisions of bare nuclei with hydrogenlike atomic systems. It gives the total cross sections, both state-selective ( $Q_{nlm}$ ,  $Q_{nl}$ ,  $Q_n$ ) and state-summed ( $Q_\Sigma$ ) for any triple  $nlm$ . Explicit computations are carried out for  $1 \leq n \leq n_{\max}$ , including all the sublevels  $l$  and  $m$  (presently, we set  $n_{\max} = 4$ ). To account for all the higher excited states with  $n > n_{\max}$ , use is made of the Oppenheimer  $n^{-3}$  scaling rule in estimating  $Q_\Sigma$ . Both colliding particles are considered with their arbitrary nuclear charges and this permits an extension which can encompass multielectron targets (heliumlike and more involved atomic systems). To simplify, we presently resort to the frozen-core approximation combined with the effective hydrogenic model for a multielectron target. The frozen-core approximation assumes that only one electron in the target is active, while the other electrons are passive and occupying the same orbitals before and after the collision. The effective hydrogenic model eliminates altogether the passive electrons through the replacement of a multielectron target by the corresponding hydrogenlike atomic system with the Slater-screened nuclear charge  $Z_r^{\text{eff}} = Z_r - \frac{5}{16}$  in lieu of  $Z_r$ . This reduces the original many-body problem to an effective three-body problem to which the foregoing analysis is directly applicable.

We employ this code to compute the state-selective as well as state-summed total cross sections ( $Q_{nlm}$ ,  $Q_{nl}$ ,  $Q_n$ ,  $Q_\Sigma$ ) and likewise for the differential cross sections [ $(dQ/d\Omega)_{nlm}$ ,  $(dQ/d\Omega)_{nl}$ ,  $(dQ/d\Omega)_n$ ,  $(dQ/d\Omega)_\Sigma$ ]. These observables are for electron capture in the  $p$ -H,  $\alpha$ -H, and

$p$ -He collisions at impact energies varying over three orders of magnitudes,  $10 \text{ keV/amu} \leq E \leq 1000 \text{ keV/amu}$ . The obtained comprehensive sets of the results are reported in the two complementary forms (tabular and graphical) that are deemed to be useful for further explorations by other authors. Within the said wide impact energy interval, the corresponding total cross sections summed through all the final bound states  $Q_\Sigma$  extend over five or seven orders of magnitudes, depending on the colliding aggregates. The state-selective and state-summed angular distributions are computed and presented for the  $p$ -H charge-exchange collisions at 60, 125, and 5000 keV. Overall excellent agreement is recorded between the BCIS-3B method and the available experimental data for total  $\{Q_{nl}, Q_n, Q_\Sigma\}$  and differential cross sections  $(dQ/d\Omega)_\Sigma$ . In particular, for capture into the spherically symmetrical  $s$  states ( $l = 0$ ), this accord within  $Q_{nl}$  occurs toward the lower edges of the intermediate range (descending to about 20 keV/amu). In the case of the final hydrogenlike  $p$  and  $d$  states with nonzero angular momentum ( $l = 1$  and 2), the BCIS-3B method for  $Q_{nl}$  is in excellent agreement with the measured cross sections down to 50 keV/amu. This is remarkable for a high-energy theory, such as the BCIS-3B method.

#### ACKNOWLEDGMENTS

N.M., I.M., and D.D. thank the Ministry of Education, Science and Technological Development of the Republic of Serbia for support under Contract No. 451-03-68/2020-14/200124. D.Ž.B. thanks Radiumhemmet (at the Karolinska University Hospital) and the City Council of Stockholm (FoUU) support through two research grants.

- 
- [1] D.Ž. Belkić, R. Gayet, and A. Salin, *Phys. Rep.* **56**, 279 (1979).
  - [2] D.Ž. Belkić, *Principles of Quantum Scattering Theory* (Institute of Physics, Bristol, 2004).
  - [3] D.Ž. Belkić, *Quantum Theory of High-Energy Ion-Atom Collisions* (Taylor & Francis, Oxford, 2008).
  - [4] D.Ž. Belkić, I. Mančev, and J. Hanssen, *Rev. Mod. Phys.* **80**, 249 (2008).
  - [5] D.Ž. Belkić, *J. Math. Chem.* **57**, 1 (2019).
  - [6] E. Ghanbari-Adivi, *J. Phys. B: At., Mol. Opt. Phys.* **44**, 165204 (2011).
  - [7] R. Shakeshaft, *Phys. Rev. A* **18**, 1930 (1978).
  - [8] X. M. Tong, D. Kato, T. Watanabe, and S. Ohtani, *Phys. Rev. A* **62**, 052701 (2000).
  - [9] S. K. Avazbaev, A. S. Kadyrov, I. B. Abdurakhmanov, D. V. Fursa, and I. Bray, *Phys. Rev. A* **93**, 022710 (2016).
  - [10] A. S. Kadyrov, I. Bray, and A. T. Stelbovics, *Phys. Rev. A* **73**, 012710 (2006).
  - [11] A. S. Kadyrov, I. B. Abdurakhmanov, I. Bray, and A. T. Stelbovics, *Phys. Rev. A* **80**, 022704 (2009).
  - [12] I. B. Abdurakhmanov, J. J. Bailey, A. S. Kadyrov, and I. Bray, *Phys. Rev. A* **97**, 032707 (2018).
  - [13] M. Zapukhlyak and T. Kirchner, *Phys. Rev. A* **80**, 062705 (2009).
  - [14] M. Baxter and T. Kirchner, *Phys. Rev. A* **93**, 012502 (2016).
  - [15] J. R. Oppenheimer, *Phys. Rev.* **31**, 349 (1928).
  - [16] H. C. Brinkman and H. A. Kramers, *Proc. Acad. Sci. Amsterdam* **33**, 973 (1930).
  - [17] D. Dollard, *J. Math. Phys.* **5**, 729 (1964).
  - [18] I. M. Cheshire, *Proc. Phys. Soc., London* **84**, 89 (1964).
  - [19] D.Ž. Belkić, R. Gayet, J. Hanssen, and A. Salin, *J. Phys. B: At. Mol. Phys.* **19**, 2945 (1986).
  - [20] G. Deco, J. Hanssen, and R. D. Rivarola, *J. Phys. B: At. Mol. Phys.* **19**, L635 (1986).
  - [21] R. D. Rivarola, J. M. Maidagan, and J. Hanssen, *Nucl. Instrum. Methods Phys. Res., Sect. B* **27**, 565 (1987).
  - [22] T. P. Grozdanov and P. S. Krstić, *Phys. Scr.* **38**, 32 (1988).
  - [23] N. Toshima and T. Ishihara, *Phys. Rev. A* **40**, 638 (1989).
  - [24] S. Alston, *Phys. Rev. A* **41**, 1705 (1990).
  - [25] L. Gulyás and G. Szabó, *Phys. Rev. A* **43**, 5133 (1991).
  - [26] D.Ž. Belkić, S. Saini, and H. S. Taylor, *Z. Phys. D* **3**, 59 (1986).
  - [27] D.Ž. Belkić, S. Saini, and H. S. Taylor, *Phys. Rev. A* **36**, 1601 (1987).
  - [28] D.Ž. Belkić and H. S. Taylor, *Phys. Rev. A* **35**, 1991 (1987).
  - [29] D.Ž. Belkić, *Phys. Rev. A* **37**, 55 (1988).
  - [30] D.Ž. Belkić, *Phys. Scr.* **40**, 610 (1989).
  - [31] D.Ž. Belkić, *Phys. Scr.* **1989**, 106 (1989).
  - [32] D.Ž. Belkić and I. Mančev, *Phys. Scr.* **42**, 285 (1990).

- [33] D. P. Dewangan and J. Eichler, *J. Phys. B: At. Mol. Phys.* **19**, 2939 (1986).
- [34] D. P. Dewangan and J. Eichler, *Nucl. Instrum. Methods Phys. Res., Sect. B* **23**, 160 (1987).
- [35] N. Toshima, T. Ishihara, and J. Eichler, *Phys. Rev. A* **36**, 2659 (1987).
- [36] F. Decker and J. Eichler, *Phys. Rev. A* **39**, 1530 (1989).
- [37] D. S. F. Crothers and L. J. Dubé, *Adv. At. Mol. Phys.* **30**, 287 (1989).
- [38] D. P. Dewangan and J. Eichler, *Phys. Rep.* **247**, 59 (1994).
- [39] B. H. Bransden and D. P. Dewangan, *Adv. At. Mol. Phys.* **25**, 343 (1988).
- [40] I. Mančev, N. Milojević, and Dž. Belkić, *Eur. Phys. J. D* **72**, 209 (2018).
- [41] Dž. Belkić, *J. Phys. B: At. Mol. Phys.* **10**, 3491 (1977).
- [42] M. Ghosh, S. Datta, and S. C. Mukherjee, *Phys. Rev. A* **30**, 1307 (1984).
- [43] S. Datta, C. R. Mandal, and S. C. Mukherjee, *Can. J. Phys.* **62**, 307 (1984).
- [44] G. C. Saha, S. Datta, and S. C. Mukherjee, *Phys. Rev. A* **31**, 3633 (1985).
- [45] M. Ghosh, C. R. Mandal, and S. C. Mukherjee, *Phys. Rev. A* **35**, 5259 (1987).
- [46] D. S. F. Crothers and K. M. Dunseath, *J. Phys. B: At. Mol. Phys.* **20**, 4115 (1987).
- [47] N. C. Deb, *Phys. Rev. A* **38**, 1202 (1988).
- [48] K. M. Dunseath, D. S. F. Crothers, and T. Ishihara, *J. Phys. B: At., Mol. Opt. Phys.* **21**, L461 (1988).
- [49] D. S. F. Crothers and K. M. Dunseath, *J. Phys. B: At., Mol. Opt. Phys.* **23**, L365 (1990).
- [50] R. Samanta, M. Purkait, and C. R. Mandal, *Phys. Rev. A* **83**, 032706 (2011).
- [51] R. Samanta, S. Jana, C. R. Mandal, and M. Purkait, *Phys. Rev. A* **85**, 032714 (2012).
- [52] S. Samaddar, S. Halder, A. Mondal, C. R. Mandal, M. Purkait, and T. K. Das, *J. Phys. B: At., Mol. Opt. Phys.* **50**, 065202 (2017).
- [53] Dž. Belkić, *Phys. Rev. A* **47**, 3824 (1993).
- [54] I. Mančev, N. Milojević, and Dž. Belkić, *Phys. Rev. A* **91**, 062705 (2015).
- [55] Dž. Belkić, *J. Math. Chem.* **47**, 1420 (2010).
- [56] R. C. Isler, *Plasma Phys. Controlled Fusion* **36**, 171 (1994).
- [57] D. M. Thomas, *Phys. Plasmas* **19**, 056118 (2012).
- [58] R. Hemsworth, H. Decamps, J. Graceffa, B. Schunke, M. Tanaka, M. Dremel, A. Tanga, H. P. L. De Esch, F. Geli, J. Milnes, T. Inoue, D. Marcuzzi, P. Sonato, and P. Zaccaria, *Nucl. Fusion* **49**, 045006 (2009).
- [59] H. Anderson, M. G. von Hellermann, R. Hoekstra, L. D. Horton, A. C. Howman, R. W. T. Konig, R. Martin, R. E. Olson, and H. P. Summers, *Plasma Phys. Controlled Fusion* **42**, 781 (2000).
- [60] Dž. Belkić, *J. Math. Chem.* **47**, 1366 (2010).
- [61] L. F. Errea, C. Illescas, P. M. M. Gabás, L. Méndez, I. Rabadán, A. Riera, and B. Pons, in *Fast Ion-Atom and Ion-Molecule Collisions*, edited by Dž. Belkić (World Scientific, Singapore, 2013), p. 231.
- [62] R. Garcia-Molina, I. Abril, and P. de Vera, in *Fast Ion-Atom and Ion-Molecule Collisions*, edited by Dž. Belkić (World Scientific Publishing, Singapore, 2013), p. 271.
- [63] M. A. Rodríguez-Bernal and J. A. Liendo, in *Theory of Heavy Ion Collision Physics in Hadron Therapy*, edited by Dž. Belkić (Elsevier, Amsterdam, 2013), p. 203.
- [64] R. D. Rivarola, M. E. Galassi, P. D. Fainstein, and C. Champion, in *Theory of Heavy Ion Collision Physics in Hadron Therapy*, edited by Dž. Belkić (Elsevier, Amsterdam, 2013), p. 231.
- [65] C. Champion, J. Hanssen, and R. D. Rivarola, in *Theory of Heavy Ion Collision Physics in Hadron Therapy*, edited by Dž. Belkić (Elsevier, Amsterdam, 2013), p. 269.
- [66] J. J. Bailey, I. B. Abdurakhmanov, A. S. Kadyrov, and I. Bray, in *State-of-the-Art-Reviews on Energetic Ion-Atom and Ion-Molecule Collisions*, edited by Dž. Belkić, I. Bray, and A. Kadyrov (World Scientific Publishing, Singapore, 2019), p. 227.
- [67] S. Guatelli, D. Bolst, Z. Francis, S. Inerti, V. Ivanchenko, and A. B. Rosenfeld, in *State-of-the-Art-Reviews on Energetic Ion-Atom and Ion-Molecule Collisions*, edited by Dž. Belkić, I. Bray, and A. Kadyrov (World Scientific Publishing, Singapore, 2019), p. 255.
- [68] Dž. Belkić, in *State-of-the-Art-Reviews on Energetic Ion-Atom and Ion-Molecule Collisions*, edited by Dž. Belkić, I. Bray, and A. Kadyrov (World Scientific Publishing, Singapore, 2019), p. 285.
- [69] I. S. Gradshteyn and I. M. Ryzhik, *Tables of Integrals, Series and Products*, 6th ed. (Academic, New York, 2000).
- [70] M. Abramowitz and I. A. Stegun, *Handbook of Mathematical Functions* (Dover, New York, 1972).
- [71] A. Erdélyi, W. Magnus, F. Oberhettinger, and F. G. Tricomi, *Higher Transcendental Functions* (McGraw-Hill, New York, 1954).
- [72] I. Mančev, N. Milojević, and Dž. Belkić, *Phys. Rev. A* **86**, 022704 (2012).
- [73] Dž. Belkić and H. S. Taylor, *Phys. Scr.* **39**, 226 (1989).
- [74] E. Filter and E. O. Steinborn, *Phys. Rev. A* **18**, 1 (1978).
- [75] P. Appell and J. Kampe de Fariet, *Functions Hypergeometriques et Hyperspheriques* (Gauthier-Villars, Paris, 1926).
- [76] G. Ryding, A. B. Wittkower, and H. B. Gilbody, *Proc. Phys. Soc., London* **89**, 547 (1966).
- [77] J. E. Bayfield, *Phys. Rev.* **185**, 105 (1969).
- [78] T. J. Morgan, J. Stone, and R. Mayo, *Phys. Rev. A* **22**, 1460 (1980).
- [79] R. F. Stebbings, R. A. Young, C. L. Oxley, and H. Ehrhardt, *Phys. Rev.* **138**, A1312 (1965).
- [80] T. J. Morgan, J. Geddes, and H. B. Gilbody, *J. Phys. B: At. Mol. Phys.* **6**, 2118 (1973).
- [81] T. Kondow, R. J. Girnius, Y. P. Chong, and W. L. Fite, *Phys. Rev. A* **10**, 1167 (1974).
- [82] E. P. Andreev, V. A. Ankudinov, and S. V. Bobashev, in *Proceedings of the 5th International Conference on Photonic, Electronic, and Atomic Collisions (ICPEAC)*, Book of Abstracts (Nauka, Leningrad, 1967), p. 309.
- [83] J. E. Bayfield, *Phys. Rev.* **182**, 115 (1969).
- [84] R. H. Hughes, E. D. Stokes, Choe Song-Sik, and T. J. King, *Phys. Rev. A* **4**, 1453 (1971).
- [85] M. P. Hughes, J. Geddes, R. W. McCullough, and H. B. Gilbody, *Nucl. Instrum. Methods Phys. Res., Sect. B* **79**, 50 (1993).
- [86] R. H. Hughes, H. R. Dawson, and B. M. Doughty, *Phys. Rev.* **164**, 166 (1967).

- [87] R. H. Hughes, C. A. Stigers, B. M. Doughty, and E. D. Stokes, *Phys. Rev. A* **1**, 1424 (1970).
- [88] J. C. Ford and E. W. Thomas, *Phys. Rev. A* **5**, 1694 (1972).
- [89] Dž. Belkić and R. Gayet, *J. Phys. B: At. Mol. Phys.* **10**, 1911 (1977).
- [90] L. W. Fite, R. F. Stebbings, D. G. Hummer, and R. T. Brackman, *Phys. Rev.* **119**, 663 (1960).
- [91] G. W. McClure, *Phys. Rev.* **148**, 47 (1966).
- [92] H. B. Gilbody and G. Ryding, *Proc. R. Soc., London, Ser. A* **291**, 438 (1966).
- [93] A. B. Wittkower, G. Ryding, and H. B. Gilbody, *Proc. R. Soc., London, Ser. A* **89**, 541 (1966).
- [94] P. Hvelplund and A. Andersen, *Phys. Scr.* **26**, 375 (1982).
- [95] P. M. Stier and C. F. Barnett, *Phys. Rev.* **103**, 896 (1956).
- [96] C. F. Barnet and H. K. Reynolds, *Phys. Rev.* **109**, 355 (1958).
- [97] L. M. Welsh, K. H. Berkner, S. N. Kaplan, and R. V. Pyle, *Phys. Rev.* **158**, 85 (1967).
- [98] U. Schryber, *Helv. Phys. Acta* **40**, 1023 (1967).
- [99] L. H. Toburen, M. Y. Nakai, and R. A. Langley, *Phys. Rev.* **171**, 114 (1968).
- [100] P. J. Martin, D. M. Blankenship, T. J. Kvale, E. Redd, J. L. Peacher, and J. T. Park, *Phys. Rev. A* **23**, 3357(R) (1981).
- [101] J. T. Park, in *Proceedings of the 12th International Conference on Photonic, Electronic, and Atomic Collisions (ICPEAC)*, Book of Abstracts (North-Holland, Amsterdam, 1982).
- [102] H. Vogt, R. Schuch, E. Justiniano, M. Shulz, and W. Schwab, *Phys. Rev. Lett.* **57**, 2256 (1986).
- [103] Dž. Belkić, *Europhys. Lett.* **7**, 323 (1988).
- [104] Dž. Belkić, *Phys. Scr.* **53**, 414 (1996).
- [105] R. D. Rivarola and J. Miraglia, *J. Phys. B: At. Mol. Phys.* **15**, 2221 (1982).
- [106] M. B. Shah and H. B. Gilbody, *J. Phys. B: At. Mol. Phys.* **11**, 121 (1978).
- [107] G. J. Frieling, R. Hoekstra, E. Smulder, W. J. Dickson, A. N. Zinoviev, S. J. Kuppens, and F. J. de Heer, *J. Phys. B: At., Mol. Opt. Phys.* **25**, 1245 (1992).
- [108] J. E. Bayfield and G. A. Khayrallah, *Phys. Rev. A* **12**, 869 (1975).
- [109] R. E. Olson, A. Salop, R. A. Phaneuf, and F. W. Meyer, *Phys. Rev. A* **16**, 1867 (1977).
- [110] M. M. Sant'Anna, W. S. Melo, A. C. F. Santos, V. L. B. de Jesus, M. B. Shah, G. M. Sigaud, E. C. Montenegro, H. F. Busnengo, S. E. Corchs, R. D. Rivarola, and L. Gulyás, *Phys. Rev. A* **61**, 052717 (2000).
- [111] S. K. Allison, *Rev. Mod. Phys.* **30**, 1137 (1958).
- [112] L. I. Pivovarov, M. T. Novikov, and V. M. Tubaev, *Zh. Eksp. Teor. Fiz.* **42**, 1490 (1962) [*Sov. Phys.-JETP* **15**, 1035 (1962)].
- [113] J. E. Bayfield and G. A. Khayrallah, *Phys. Rev. A* **11**, 920 (1975).
- [114] P. Hvelplund, J. Heinemeier, E. Horsdal-Pedersen, and F. R. Simpson, *J. Phys. B: At. Mol. Phys.* **9**, 491 (1976).
- [115] R. Cline, P. J. M. van der Burgt, W. B. Westerveld, and J. S. Risley, *Phys. Rev. A* **49**, 2613 (1994).
- [116] R. Hippler, W. Harbich, M. Faust, H. O. Lutz, and L. J. Dubé, *J. Phys. B: At. Mol. Phys.* **19**, 1507 (1986).
- [117] R. Hippler, W. Harbich, H. Madeheim, H. Kleinpoppen, and H. O. Lutz, *Phys. Rev. A* **35**, 3139 (1987).
- [118] R. J. Conrads, T. W. Nichols, J. C. Ford, and E. W. Thomas, *Phys. Rev. A* **7**, 1928 (1973).
- [119] M. C. Brower and F. M. Pipkin, *Phys. Rev. A* **39**, 3323 (1989).
- [120] R. A. Cline, W. B. Westerveld, and J. S. Risley, *Phys. Rev. A* **43**, 1611 (1991).
- [121] J. L. Edwards and E. W. Thomas, *Phys. Rev. A* **2**, 2346 (1970).
- [122] B. M. Doughty, M. L. Goad, and R. W. Cernosek, *Phys. Rev. A* **18**, 29 (1978).
- [123] J. F. Williams, *Phys. Rev.* **157**, 97 (1967).
- [124] P. J. Martin, K. Arnett, D. M. Blankenship, T. J. Kvale, J. L. Peacher, E. Redd, V. C. Sutcliffe, J. T. Park, C. D. Lin, and J. H. McGuire, *Phys. Rev. A* **23**, 2858 (1981).
- [125] M. B. Shah and H. B. Gilbody, *J. Phys. B: At. Mol. Phys.* **18**, 899 (1985).
- [126] M. B. Shah, P. McCallion, and H. B. Gilbody, *J. Phys. B: At., Mol. Opt. Phys.* **22**, 3037 (1989).
- [127] E. Hylleraas, *Z. Phys.* **54**, 347 (1929).
- [128] J. N. Silverman, O. Platas, and F. A. Matsen, *J. Chem. Phys.* **32**, 1402 (1960).
- [129] K. E. Banyard and B. J. Szuster, *Phys. Rev. A* **16**, 129 (1977).
- [130] Dž. Belkić, R. Gayet, J. Hanssen, I. Mančev, and A. Nuñez, *Phys. Rev. A* **56**, 3675 (1997).
- [131] A. W. Weiss, *Phys. Rev.* **122**, 1826 (1961).